Modelling Flexural Performance of Hollow Pultruded FRP Profiles

Mohammad Alhawamdeh*[1], Omar Alajarmeh[1], Thiru Aravinthan[1], Tristan Shelley[1], Peter Schubel[1], Ali Mohammad[2], Xuesen Zeng[1]

*Corresponding author: Mohammad.Alhawamdeh@usq.edu.au, University of Southern Queensland West Street Toowoomba Qld 4350 Australia

[1] University of Southern Queensland, Centre for Future Materials, Toowoomba Queensland Australia 4350

[2] Wagners Composite Fibre Technologies, Wellcamp Queensland Australia 4350

ABSTRACT

Hollow Pultruded Fibre-Reinforced Polymer (PFRP) profiles, as novel construction material, require further development of design tool to broaden the applications. This paper proposes a combined experimental and numerical methodology as a design tool to investigate the failure modes of these profiles under four-point bending. Two different profiles, each with 10 samples, were tested until failure and were used to validate the numerical model. A finite element model was built based on a fast-convergence incremental approach that suits flexural loading and reduces the computational cost. The validated model was used to study the failure sequence thoroughly and perform an extensive parametric study on the design parameters. Each geometric parameter was studied individually first to determine the relevant levels for each parameter in the full factorial study. A full factorial design of experiment was used to capture the critical parametric interactions with over 81 numerical models. The design rules and recommendation were established for the optimal flexural behaviour of hollow box PFRP profiles to withstand local buckling of the top flange.

Keywords: Hollow GFRP profiles, Finite element analysis, Local buckling, Flexural failure.

1. INTRODUCTION

The civil infrastructure sector witnessed an immerging use of hollow Pultruded Fibre-Reinforced Polymer (FRP) profiles as structural members, such as beams and girders in buildings and bridges [1,2]. One of the most prominent developments on pultrusion was the introduction of pulwinding technology, at which off-axis wound fibres are pulled along with the axial fibres. The presence of wound fibres improves the delamination resistance, optimise the transverse properties, and enhance the post-processing endurance, such as jointing and bolting [3,4]. Moreover, it increases the buckling load capacity of the profiles [5,6]. Hollow box PFRP profiles manufactured by pulwinding possess tailorable design parameters including layup parameters (wound fibre angle, axial-to-wound fibres ratio, and stacking sequence) and geometric parameters (wall thickness, cross-sectional aspect ratio, and corner radius). These parameters govern the profile response to local buckling, which is a dominant failure mode of the top flange of hollow PFRP beams because of their anisotropic and slender nature [7–11]. Local buckling of hollow box PFRP profiles differs depending on the loading condition. The four walls buckle under axial compression loading while only the top flange, and partially the webs, would buckle under bending loading [12,13]. Thus, the buckle half-wavelength under axial compression is smaller compared to the response under bending. Smaller buckle half-wavelength means that more buckling waves will appear due to the lower restraint provided by the other walls, since they are also buckled, in compression loading [14–16]. Consequently, local buckling of walls is more critical under axial compression compared to bending. Therefore, it is important to investigate the design parameters of the profile under the loading condition, which the profile is intended for, to reach a clear understanding of the profile limitations and how to alleviate them. Studying the effect, contribution, and interaction of these design parameters under bending is going to provide guidelines on the design for

manufacturing and recommended configurations of pulwound hollow box PFRP profiles to fully utilise their potentials and overcome local instabilities.

The layup properties significantly affect the structural performance of laminated composite beams [17,18]. Several studies were undertaken to study these properties and their effect on the local buckling capacity. The buckling load capacity of filament-wound Glass Fibre-Reinforced Polymer (GFRP) profiles subjected to compression was increased by 20% when the winding angle was increased from 30^o to 60^o [19]. The effect of the fibres orientation on the buckling load of FRP composite profiles made with unidirectional [20], angle-ply, and cross-ply [21,22] layups and subjected to axial compression was studied numerically. It was found that the critical buckling load decreased by 35% when the fibre angle increased from 10° to 30° for the unidirectional composite profile [20]. The cross-ply laminate was observed to sustain a larger buckling load than angle-ply laminate when the fibre angle is larger than 30^o[21,22]. In general, balanced and symmetric laminate is preferred to minimise the manufacturing imperfection and limit the elastic coupling effect and warp [23–25]. It was found that adding off-axial fibres along with axial fibres will enhance the local buckling capacity of composite laminated beams [26]. However, no studies were found to address the optimal ratio of these fibres for pulwound profiles.

Regarding the geometric parameters, the effect of the wall thickness of T and C shape PFRP beams on the local buckling capacity of the compression flange was studied under uniformly distributed bending load [27]. It was found that the local buckling capacity of the compression flange is inversely related to its slenderness. The buckling capacity was reduced by 37% when the wall thickness was decreased from 12 mm to 6 mm. The buckling behaviour of hollow box pultruded GFRP beams subjected to four-point bending was investigated for different flange slenderness values made by maintaining the same thickness and changing the flange width [28]. The local buckling moment of the flange was decreased by 49% due to the reduction in

the flange slenderness from 12 to 6. No limitations or inflection points of failure modes of the top flange were reported for such profiles.

The effect of the height-to-width ratio on the critical buckling load of hollow box PFRP profiles subjected to compression was studied [29]. The critical buckling capacity of the top flange was increased by 32% when the height-to-width ratio was increased from 1 to 3 (maintaining the same cross-sectional area). Moreover, the local buckling failure map of the flange and web for different cross-sectional aspect ratios of adhesively bonded laminated box beam was obtained under three-point bending [30]. However, the inflection point between the local buckling and the compressive failure of the top flange, and the interaction between this parameter and the other geometric parameters were not reported.

The corners are considered critical zones in PFRP beams as they need support to enhance the structural performance and avoid premature failure due to stress concentration [31–33]. The corner of I-shape PFRP beams subjected to four-point bending was enhanced by adding hand-layup fillets (38 mm) on the top flange-web junctions [34]. The buckling resistance was enhanced by 50% due to the increase in rotational stiffness and the failure mode was shifted from buckling of the top flange to compressive failure of fibres. Nevertheless, no studies were found on the corner geometry of hollow box PFRP profiles and its configuration that separates the two failure modes.

After reviewing the relevant literature, it appears that most of the design parameters were studied individually to obtain their effect only. Moreover, part of them was studied under compression, which may not reflect the exact behaviour under bending. In addition, their contribution and interactions were not quantified. Practical design guidelines rely on these two fundamental aspects to focus on the most significant parameters and obtain the optimal configuration of the hollow PFRP profiles. Furthermore, the influence of these design

parameters on the failure sequence of these profiles under bending has not been characterised, especially the corners. The finite element method (FEM) is considered as an excellent option to thoroughly study the failure mechanism of hollow box PFRP profiles and carry out parametric studies on the design parameters due to its capability of handling combined failure problems and complex geometries [35–45].

After studying the failure mechanism of hollow box PFRP profiles under axial compression [16], this paper is going to investigate the failure mechanism of these profiles under bending experimentally and numerically. The incremental modelling approach presented by the authors [16] for compression was further developed with fast convergence under flexural loading while improving the computational efficiency. The validated model is going to be used to study the effect, contribution, and interaction of the design parameters under four-point bending by full factorial design of experiment. These parameters are three layup parameters (wound fibre angle, axial-to-wound fibres ratio, and stacking sequence) and three geometric parameters (wall thickness, cross-sectional aspect ratio, and corner radius). Each geometric parameter was studied individually to generate the failure map of hollow PFRP profiles and to device up the applicable levels for each parameter in the full factorial study. The current study demonstrates a comprehensive novel approach to the design process of hollow PFRP profiles and maximises the material efficiency for bending applications.

2. EXPERIMENTAL PROGRAM

An experimental program was undertaken on hollow box PFRP profiles to validate the numerical model that will be used to investigate the design parameters through a series of parametric studies.

2.1 Materials and structures

The studied PFRP profiles were manufactured by Wagners CFT using pulwinding technology. These square profiles are made of E-glass fibre & Vinyl-Ester polymer resin with the layup and geometric properties shown in Table 1, as provided by the manufacturer. Fig. 1 depicts the cross-sections of these profiles.

2.2 Test setup

The flexural behaviour of the hollow box PFRP profiles was examined under a four-point bending test configuration. Ten specimens of each profile with a length of 2435 mm and a clear span of 2235 mm were prepared to be loaded until failure. The span-to-depth (L/D) ratio was 22.35 and 17.88 for the S-100×100×5.2 and S-125×125×6.4 profiles, respectively. Fig. 2 shows the test configuration along with the used dimensions. These values were considered in compliance with ASTM D7249/D7249M specifications to avoid shear effect and localised transverse damage and to obtain pure bending behaviour [46–49]. Simple (Pin-roller) steel supports were used at the ends and the load was applied through two steel plates, each of them covers 100 mm of the beam length, as shown in Fig. 3.

A Linear Variable Differential Transducer (LVDT) unit was mounted at the mid-span of the bottom flange to record the deflection of the beam. The loading cells were connected to a data acquisition system to obtain the load values. A quasi-static loading-rate of 10 mm/min was applied on the beam top flange through the two loading plates.

3. FINITE ELEMENT MODELLING

3.1 Background

Abaqus/CAE 2019 was used to simulate the two hollow box PFRP profiles. The stiffness properties controlling the elastic behaviour of the box profiles were defined through the elastic lamina material definition. This definition is suitable for two-dimensional plane stress

formulation members such as laminated shells [50]. The mechanical properties of an E-glass/Vinyl-ester lamina with fibre volume fraction (V_f) of 0.6 (as provided by the manufacturer) are shown in Table 2. The rule of mixture was used to calculate the elastic modulus in the fibre direction (E_1). Whereas the empirical equations [51,52] were applied to obtain the transverse elastic modulus (E_2), the in-plane shear modulus (G_{12}), and the out-of-plane shear modulus (G_{23}). The value of (G_{13}) was assumed to equal the value of (G_{12}) because unidirectional laminae behave as transversely isotropic materials [37].

3.2 Local buckling and Progressive failure behaviours

The entire structural behaviour of the hollow box PFRP beams was modelled, including local buckling and progressive failure. A nonlinear geometric analysis was performed using the Newton method in Abaqus/Standard along with the large displacement formulation to capture the deformations accompanying the buckling behaviour and consider all the nonlinearity effects (from geometry, material failure, and boundary conditions). The adaptive automatic stabilisation scheme was used to damp the severe nonlinearities, which accompany buckling and prevent termination errors. To eliminate the dependency of the incremental solution on the number of increments when buckling is dominant, the maximum increment size was reduced down to 0.35% of the total step time until convergence was achieved with a tolerance of 5% between the load capacities of the successive increment sizes. This novel modelling approach combining the local buckling, post-buckling, and progressive failure behaviours was addressed in detail and verified in previous research under compression [16]. However, when studying the convergence at the current problem under bending, the solution was noticed to converge faster against the number of increments compared to compression, as shown in Fig. 4. The numerical ultimate buckling stress converged at 1.33% of the total step time with the same tolerance on the load capacity provided for compression. Considering this observation, the analysis can be performed faster even with the larger number of elements (the element size is

constant under both loading conditions) due to the four times larger increment size compared to compression. This finding was related to the severity of local buckling under compression compared to bending. A smaller increment size was needed to capture the instability on the four walls and converge the results under compression compared to one wall under bending.

Hashin damage model [50] was utilised to simulate the progressive failure of the lamina constituents (fibres and matrix). Four different failure modes are considered in the model: rupture of fibre in tension, buckling and kinking of fibre in compression, cracking of matrix under transverse tension and shearing, and crushing of matrix under transverse compression and shearing. Three components are required for the model to be defined, which are the damage initiation criteria, damage evolution response, and damage stabilisation scheme. For the damage initiation criteria, the strength limits of a unidirectional E-glass/Vinyl-Ester lamina were extracted from literature for the same profiles [51]. These values are shown in Table 2. The superscripts C and T symbolise compression and tension, and the notations X, Y, and S refer to the longitudinal, transverse, and shear strength values. The damage evolution algorithm is triggered when the damage initiation criterion for any of the four failure modes is met at any element. This algorithm is based on the energy release, which equals the area under the equivalent stress-displacement curve of the element [50]. Thus, the maximum energy needed to cause failure in the element; the fracture energy, should be assigned for each failure mode. The fracture energy values of E-glass/Ly556 epoxy lamina were used [53] since no data was found in the literature for each failure mode of the studied lamina. These values are shown in Table 2 with double subscript notation, consisting of L and T as the first subscript that refers to the longitudinal and transverse directions and the second subscript of T and C that denotes to the tension and compression. The damage stabilisation scheme was used to overcome the difficulties of results convergence when modelling material failure by making the tangent stiffness matrix positive for adequate time increments. The solver introduces a viscosity

coefficient to the damage evolution equations to relax the time in the vicious system [50]. The optimal viscosity coefficient values for the four failure modes was specified by a sensitivity study with a range of $[1 \times 10^{-6} - 1 \times 10^{-2}]$ sec. A viscosity coefficient of 1×10^{-3} sec was used for each failure mode depending on the energy balance of the models.

3.3 Mesh, boundary conditions, and loading condition

The quadrilateral (8-node) in-plane general-purpose continuum shell (SC8R) element was used to model the hollow box PFRP profiles. This three-dimensional element presents the best option for the studied PFRP profiles and their geometric parameters. It allows geometric modifications through the thickness such as tapering or thicken the corner geometry. Moreover, it simulates the through-thickness behaviour more accurately than conventional shells due to its through-thickness seeding feature [50]. The number of elements through the thickness was increased by local seeding to greatly reduce hourglass modes and capture the kinematic response accurately. The suitable element size allowing the results to converge was obtained through a mesh sensitivity study. For both S-100×100×5.2 and S-125×125×6.4 PFRP profiles, five elements through-thickness and 5 mm element edge length were used. The mesh around the corners was refined by locally assigning five elements to this critical zone of stresses concentration.

The supports were simulated by assigning boundary conditions at the ends of the beams. The translational degrees of freedom were restrained at both ends with only free axial displacement (with respect to the beam axis) at one end allowed free to move to model the roller behaviour and allow for pure axial shortening-transverse deflection deformation without unrealistic intervention from supports in the flexural stiffness. In addition, all the rotational degrees of freedom were free to rotate. The loading plates were simulated using three-dimensional discrete rigid solid parts with dimensions of 150×100×20 mm. These plates were connected to the top

flange of the hollow box beams over a 100 mm length using a tie constraint definition. The loading process was simulated by imposing a vertical translational movement on the loading plates through a displacement-control loading of 10 mm/min.

4. MODEL VALIDATION

The models' validity was assessed by comparing the FEM results versus the experimental results in terms of the load-deflection curves and the failure mode. In addition, the numerical and experimental buckling loads were compared to the theoretical buckling loads of the most cited equations in the literature. The validated models assisted in understanding the failure sequence and its triggering mechanism.

4.1 Local buckling load capacity of the hollow box PFRP profiles

The studied hollow box PFRP profiles were analysed theoretically [12,14,15,37] to define the triggering failure mode and then assign the appropriate theoretical equations to be compared with the current study results. Table 3 shows the theoretical results compared to the experimental and numerical results. Local buckling of walls, due to in-plane compression, controls the failure mode since its capacity is the minimum value among the theoretical results and the only capacity that is lower than the experimental and numerical results. Nevertheless, the theoretical calculations proved to be conservative with a high error of 24.9% and 36.8% between the theoretical and experimental load capacities for S-100×100×5.2 and S-125×125×6.4 beams, respectively. This finding agrees with the same literature calls regarding the inaccuracy of these empirical equations and the need to develop them to be more accurate. The buckling stress-to-longitudinal modulus ratio ($(\sigma_{cr})/(E_L)$) of the walls was assessed to check whether the top flange or the webs buckle first. For both profiles, $(\sigma_{cr})_{flange}/(E_L)_{flange} < (\sigma_{cr})_{web}/(E_L)_{web}$, which indicated that the compression flange will buckle before the webs [14]. This finding aligns with the next section conclusions regarding the failure sequence.

After confirming the theoretical failure mode, the numerical and experimental buckling stresses were compared to the most cited theoretical equations used to estimate the local buckling stress $(\sigma)_{cr}$ of an orthotropic laminated plate (the compression flange in this study). The theoretical formulas assume the top flange to be clamped along the beam length and subjected to uniaxial compressive loading along its width. This assumption can be justified in this research by the high fibre volume fraction and the continuation of the wound fibres around the corners [54]. The results of this comparison are shown in Table 4. The FEM results were the highest since they reflect the behaviour of an intact beam, while the theoretical results were lower than both experimental and numerical results as they were built on conservative assumptions (neglecting the shear deformations) for simple formulas and safe design [11]. Nevertheless, a good agreement was found between these values.

4.2 Load-deflection curves and failure mode

The numerical versus experimental load-deflection curves are shown in Fig. 5. In general, the hollow PFRP beams exhibited linear elastic behaviour experimentally and numerically until the ultimate load. The agreement between the curves is very good in terms of the flexural stiffness (EI/L^3) and the ultimate load capacity. The variation in the flexural stiffness between the numerical and average experimental results was 3.5% and 2.7%, with a standard deviation of 29.4 N/mm and 142.6 N/mm for the experimental values, for S-100×100×5.2 and S-125×125×6.4 beams, respectively. The numerical ultimate load varied by 10.3% and 5.6% from its corresponding average experimental value, with a standard deviation of 4.1 kN and 1.5 kN for the experimental values, for S-100×100×5.2 and S-125×125×6.4 beams, respectively.

The failure sequence started by local buckling of the top flange at 95.5% of the ultimate load (42.6 kN and 92.9 kN for S-100×100×5.2 and S-125×125×6.4 beams, respectively). The localised waviness occurred at the mid-span of the beams, between the two loading points, and

propagated until the ultimate load was reached, as shown in Fig. 6 (a) that shows the top flange deflected shape of the S-100×100×5.2 beam using the numerical results. Hashin damage initiation criteria of fibre by compression and matrix by tension were used to track the waviness extent, as shown in Fig. 7 that presents the failure sequence of the S-100×100×5.2 beam. Moreover, Fig. 7 (b) shows the agreement between the numerical and experimental buckling mode at the ultimate load point. As the top corners were resisting the load, they exhibited tensile damage of matrix accompanying the buckling of the top flange. The local buckling then extended to the webs causing more damage. Nevertheless, the flange-web junction maintained its rotational stiffness (evident by an angle of 90°) to resist the buckling transfer from the top flange to the webs until the beam collapses, as shown numerically in Fig. 6 (b) and Fig. 6 (c). These figures show two cross-sections, A-A and B-B, taken for the S-100×100×5.2 beam at the ultimate load point, as shown in Fig. 6 (a). This behaviour was attributed to the continuous wound fibres around the corners. These wound fibres resisted the cracks along the axial fibres and encountered delamination at the corners.

Afterwards, the localised waviness subsided when the collapse occurred at the top flange due to compressive failure of fibres, after tensile failure in the matrix. Fibres spalling and delamination of the top flange and webs occurred at the mid-span of the beams. The output variable (HSNMTCRT), which refers to the matrix failure by tension, was used to track the delamination of the beams after the collapse, as shown in Fig. 8. There was a concern that this experimental test setup might potentially cause localised premature damage of the specimens at the loading points by the metallic plates. However, the finite element models, with the simulation of the exactly same experimental setup, showed no sign of pervasive stresses concentration around the loading plates. Moreover, the buckling occurred before any sign of premature failure, either experimentally or numerically. Thus, this test setup was appropriate for the current study.

5. DESIGN OF EXPERIMENTS

The hollow box S-100×100×5.2 profile was selected for the parametric studies and the geometric parameters were normalised to produce universal results regardless of the profile's size. Reduced Design of experiment (DOE), such as the Taguchi method, is only valid to study the expected interactions since they have to be assigned before the analysis is performed. Consequently, full factorial DOE was used for all the parametric studies in this research to cover all the possible interactions between the studied parameters [55]. The DOE and the analysis of the numerical results were performed by Minitab 19 statistical analysis software. Three parametric studies, each one has three parameters, were designed to study the effect, relative contribution, and interactions of the parameters. The first study was undertaken on the layup parameters (wound fibre angle, axial-to-wound fibres ratio, and stacking sequence), while the second parametric study was performed on the geometric parameters (wall thickness, cross-sectional aspect ratio, and corner radius). The third parametric study was carried out on the geometric parameters of the flange-web junction (flange slenderness, web slenderness, and corner radius). The studied parameters were divided into these groups to reduce the huge size of the experiment matrix and the enormous computational cost. In all the parametric studies, the fibre volume fraction (V_f) was kept constant at 0.6 with the mechanical properties of an E-glass/Vinyl-ester lamina shown in Table 2. The layup parameters (wound fibre angle, axial-to-wound fibres ratio, and stacking sequence) were studied and found to be negligible compared to the geometric parameters. The total contribution of the layup parameters on the flexural stiffness (EI/L^3) and strength was 15.7% and 7.8%, respectively. Consequently, this research will focus more on the geometric parameters and their interactions under bending since they significantly control the structural performance of hollow PFRP profiles and since they are recognised more internationally in structural design approaches. Only the second and third

parametric studies on the geometric parameters and flange-web junction parameters, respectively, will be discussed following.

5.1 Level settings of geometric parameters

The profile's stability and its failure mode are dominated by the geometric parameters [37,56]. Thus, each geometric parameter was investigated independently (when a parameter is studied, the others remain constant) to locate any inflection points in the failure mode and assess the practical levels range of each parameter to be applied in the geometric factorial parametric study. The layup properties (wound fibre angle, axial-to-wound fibres ratio, and stacking sequence) were maintained constant across all these individual parametric studies and in the geometric parametric study with the values currently used in production, as shown in Table 1.

The wall thickness was studied by altering its value from 4.6, 5.2, 5.8, 6.4, 7.0, 7.6, to 8.2 mm. The numerical results of the wall thickness effect on the hollow box beam are shown in Fig. 9. These values were normalised to the flange width (b) to obtain the wall slenderness (b/t). The failure mode was shifted from local buckling to compressive failure of the top flange at an inflection point of b/t = 16.4. The flexural strength is greatly reduced, and the failure occurs before reaching the ultimate material strength when local buckling controls. For instance, the numerical compressive strength of the S-100×100×5.2 profile was 324.2 MPa, while the ultimate material strength from the coupons test reached up to 445 MPa [57]. Due to instability, the compressive strength of the top flange was reduced to 0.67 of the material failure strength. According to the numerical results, the compressive strength is increased up to 440 MPa when the wall thickness is increased up to 6.4 mm, and the failure mode is shifted from local buckling to compressive failure at the top flange.

The chosen levels of the wall thickness for the geometric parametric study were assigned to gradually shift the failure mode from local buckling to compressive failure to capture any

differences in the response along with the different failure modes. Consequently, wall thicknesses of 4.6, 5.2, 5.8 mm were selected, as shown in Table 5.

Investing in the section height of PFRP rectangular beams is a practical solution to enhance their flexural performance by increasing their moment of inertia [12,15,58,59]. The effect of changing the cross-sectional height and width (while maintaining the same cross-sectional area) was studied here by introducing the height-to-width ratio (h/b) as a design parameter. The studied values of h/b ratio were 1, 1.25, 1.5, 1.75, 2, 2.25 ,2.5 ,2.75 ,3, 3.5, and 4. The numerical results are shown in Fig. 10. The load capacity increased when the h/b ratio was increased. This observation agrees with the findings of [21]. It was inferred that the reduction in the unsupported width of the top flange was the reason as it enhanced its buckling resistance. The inflection point between the failure modes was h/b=1.5, at which the flexural strength of the beam was enhanced by 30.4%. Another inflection point was found at h/b=3, at which the failure mode was shifted from compressive failure of the top flange to local buckling of the webs. This was attributed to the increase in the unsupported height of the webs, which reduced their local buckling capacity below the material ultimate strength of the flange and resulted in a reduction in the overall flexural strength of the beam.

The chosen h/b ratios for the geometric parametric study were 1.0, 1.25, and 1.5. These values were selected to track the changes in the structural performance when moving the failure mode from local buckling to compressive failure of top flange, as shown in Table 5.

Hollow box PFRP profiles are usually manufactured with fillet corners to minimise resin-rich zones, facilitate the pulling process, reduce the stresses concentration, and avoid wound fibres fracture under high pulling force at these corners [14,37,58,60,61]. The effect of the corner geometry on the structural performance of hollow box PFRP beams was studied here by assessing the outer and inner corner radii. First, the outer corner radius (R) was investigated

while keeping the inner corner radius (r) constant. The tested values of the outer corner radius were 5, 10, 15, 20, 25, 30, 35, and 40 mm, and their numerical results are shown in Fig. 11. The section change from box to circular shape was tracked by normalising the outer corner radius with respect to the wall width (b/R). Increasing the outer corner radius resulted in a reduction of the flexural stiffness (EI/L^3) due to the decrease in the moment of inertia of the section. The profile lost approximately 1.2% of its flexural stiffness for each 1 mm increase in its outer radius. In addition, the moment capacity of the beam deteriorated even though the failure mode shifted from local buckling towards compressive failure of the top flange (due to the increase in the circumferential confinement and the uniform distribution of stresses). This was attributed to the reduction in the cross-sectional area of the top flange, which prevented it from attaining higher moment capacity even though its compressive strength has reached the ultimate material strength. The top flange lost 37.5% of its cross-sectional area at the inflection point (b/R = 4), where the change in the failure mode occurred.

Alternatively, a proposition was introduced by keeping the outer radius (R) at its minimum applicable value from the manufacturing perspective and increasing the inner radius (r) of the corner with axial fibres. A new parameter of the corner geometry was presented, namely the corner inner-to-outer radii ratio (r/R). This parameter was investigated with a range of values starting at 0.5, 1.0, 1.5, 2.0, 2.5, 3.0, to 3.5. The numerical results of investigating these values are shown in Fig. 12. This solution maintained the box shape and enhanced the flexural stiffness (EI/L^3) due to the increase in the cross-sectional area of the profile. The flexural strength increased, and the failure mode shifted from local buckling to compressive failure of the top flange at r/R = 2.5 due to the reduction of the unsupported width of the top flange and the increase in the corners restraint.

The corner inner-to-outer radii ratio was nominated for the geometric parametric study to investigate its relative contribution and interaction to the other geometric parameters. The

selected levels were 0.5, 1.0, and 2.0, as shown in Table 5. These values were chosen to track the structural performance as the failure mode moves gradually from local buckling to compressive failure of the top flange.

5.2 Level settings of flange-web parameters

After studying the profile's overall geometry, the flange-web geometry is investigated here. The effect of the flange slenderness (b/t_f) and web slenderness (h/t_w) on the failure mode is examined to set up their levels in the full factorial study.

The flange slenderness was assessed by changing its thickness from 2.8, 3.4, 4, 4.6, 5.2, 5.8, 6.4, 7, to 7.6 mm. Increasing the flange thickness increased the buckling strength since the associated slenderness ratio was decreased and the flange stability increased, as shown in Fig. 13. Similar behaviour was observed when studying the web slenderness with the same range of thickness values, as shown in Fig. 14. However, while the failure mode was shifted from local buckling of the top flange to compressive failure of top flange when the flange slenderness ratio was reduced ($b/t_f \leq 15.6$), the failure mode moved from local buckling of top flange and webs towards a compressive failure of corners when the web slenderness ratio was reduced ($h/t_w \leq 13.2$). It was inferred that the high rigidity provided by the thick webs redistributed the stresses from the top flange towards the top corners, thus preventing the stresses in the flange from reaching the buckling strength. This behaviour highlights the significance of the flange and web interaction and the importance of their junction (top corners) in shaping the profile failure mode under bending. Moreover, the threshold (inflection) point of failure modes was varying depending on the examined slenderness ratio. It was at $h/t_w = 13.2$, $b/t_f = 15.6$, or $b/t = 16.4$ (section 5.1), which clearly shows the interaction between the flange and web slenderness in terms of the buckling performance. A thicker web would be needed to stabilise the thin top flange and transfer the failure towards the corners. Alternatively, a thicker flange with thin webs can be used to eliminate local buckling in the beam. Increasing the thickness of

the flange and web would shift the failure mode at a higher slenderness ratio compared to increasing the thickness of either the flange or the web.

The corner inner-to-outer radii ratio (r/R) was also nominated for the flange-web parametric study to investigate its relative contribution and interaction to the flange and web slenderness. The selected levels were 0.5, 1.0, and 2.0, as shown in Table 6. The chosen values of the flange and web thickness (4.6, 5.2, and 5.8 mm) and r/R ratio were assigned to assess the flange-web junction performance as the failure mode moves gradually from local buckling to compressive failure of fibres. The layup properties (wound fibre angle, axial-to-wound fibres ratio, and stacking sequence) were maintained constant in this parametric study with the values currently used in production, as shown in Table 1.

6. DOE DISCUSSION

The effect of the design parameters on the structural behaviour of the hollow box PFRP beam was assessed depending on the two main responses in flexural design, namely, the flexural stiffness (EI/L^3) and strength. The contribution (significance) of each design parameter was calculated statistically by the Two-way ANOVA (analysis of variance) using Minitab 19 statistical analysis software. Also, the main effect and interaction plots were introduced to depict the effect and interaction of each design parameter, respectively. These plots display the averaged values for the levels of each parameter [62]. The full list of the design matrices and numerical results of the parametric studies are presented in Appendix A.

6.1 Effects of the geometric parameters

The contribution of each geometric parameter on the flexural behaviour of the hollow box PFRP beam is shown in Table 7 that shows the two-way ANOVA model results. The flexural stiffness (EI/L^3) increased by 17.7% per 1 mm increase in the wall thickness, by 48.1% when h=2b, and by 16.6% per 1.0 increment in r/R ratio due to the enhancement on the moment of

inertia. The cross-sectional aspect ratio was the most significant parameter affecting the flexural stiffness (EI/L^3) by contributing double of what the other two parameters contributed. This was attributed to its higher influence on the moment of inertia of the section. Besides that, the corner radii ratio contributed the most to the flexural strength of the beam followed by the wall thickness then the h/b ratio. It was inferred that the increase in the corners restraint when the r/R ratio is increased presents the largest impact on the buckling resistance of the top flange due to the increased rigidity transferred from the web to the flange and to the effect of a large r/R ratio on reducing the effective buckling width of the flange. Moreover, the enhancement in the flexural strength when the flange thickness was increased was superior to its counterpart resulting from reducing the unsupported width of the top flange. This was attributed to the exponential effect of the wall thickness on the buckling capacity of the flange [63]. For strength-controlled design, investing in r/R ratio will obtain the optimal design compared to increasing the top flange thickness or decreasing its width (b).

The top flange slenderness was reduced and its stability was enhanced when the wall thickness was increased, which obtained more strength across all h/b and r/R ratios, as shown in Fig. 15 (a) and Fig. 15 (b). Alternatively, reducing the top flange width, by increasing the h/b ratio, resulted in a reduction of its slenderness and an improvement of its stability and strength, as shown in Fig. 15 (c) for all r/R ratios.

The three geometric parameters exhibited significant interactions with each other. The first interaction was between the wall thickness and h/b ratio, as shown in Fig. 15 (a). Increasing the h/b ratio for a thinner profile resulted in a significant enhancement of the flexural strength. Whereas for a thicker profile, the effect of the h/b ratio on the flexural strength is diminishing. It was inferred that the effect of the wall thickness on the failure mode was the reason. Local buckling is dominant at thin walls, which makes the reduction of the flange width due to the increase of h/b ratio more influential on its stability and strength. When the wall thickness is

increased, the failure mode shifts towards compressive failure of the top flange at the ultimate material strength, which is independent of the flange width. Wall slenderness of $b/t \leq 16.4$ obtains the most stable configuration for hollow square profiles, while a hollow rectangular profile with flange slenderness of $b/t > 16.4$ needs $h/b \geq 1.5$ to attain its optimal configuration. Both these configurations will exhibit compressive failure of the top flange with the ultimate material strength.

The second interaction was observed between the wall thickness and the corner radius, as shown in Fig. 15 (b). The flexural strength was effectively increased when the r/R ratio was increased for the slender flange profile. However, when the wall thickness is increased and the failure mode moves from local buckling to compressive failure of the top flange, the corner radius effect of the strength decreasing. Similarly to the first interaction, the effect of the wall thickness on the failure mode was the reason. Consequently, it is recommended to manufacture thin PFRP profiles ($b/t > 16.4$) with $r/R \geq 2.5$ to avoid local buckling of the top flange and reach the ultimate material compressive strength. Contrarily, thicker profiles ($b/t \leq 16.4$) can be manufactured with $r/R \leq 1$ since they already overcome local buckling with their low flange slenderness. This configuration does not require large corners (large r/R ratio) and alleviates the manufacturing defects resulting from it such as fibre wrinkling and resin-rich zones [64].

The third interaction was between the h/b ratio and r/R ratio, as shown in Fig. 15 (c). The effect of the r/R ratio on the flexural strength of the square profile ($h/b = 1$) is notable while it is decreasing for the rectangular profile ($h/b > 1$). The hollow square profile is more prone to local buckling of the top flange compared to its counterpart (having the same cross-sectional area) rectangular profile due to the wider flange width. Thus, increasing the r/R ratio influentially increases the flexural strength of the hollow square profile compared to the rectangular profile. It is recommended to use $r/R \geq 2.5$ for thin square profiles while $r/R < 2$ can be used for thin rectangular profiles to mitigate manufacturing defects resulting from a

large r/R ratio. These two configurations will eliminate local buckling of the thin flange (b/t > 16.4) and maximise the flexural strength of the profile.

The interaction between local buckling and compression was studied by introducing an adimensional parameter (γ) to reflect the combined effect of the geometric parameters on these two failure modes. This parameter was defined as the ratio of the flexural strength of the profile (σ) to the ultimate material strength of the profile (σ_u) extracted from coupon tests [57]:

$$\gamma = {}^{\sigma}/_{\sigma_u} = f({}^{b}/_{t}, {}^{h}/_{b}, {}^{r}/_{R}) \quad (1)$$

The failure mode of the profile is a compressive failure of the top flange when γ = 1, while it is local buckling when γ < 1. The study on the geometric parameters was extended to plot γ versus the geometric parameters, as shown in Fig. 16. The effect of the interaction of the geometric parameters on the buckling capacity and the failure mode is significant and should be considered during the design process. The shape of the buckling curve was changed from concave up at small r/R and h/b ratios to concave down when r/R and h/b ratios were increasing. The failure mode started to shift closer to compressive failure of the top flange as the out-of-plane waviness accompanying buckling was diminishing at h/b = 1.25 and r/R = 1 design (the red curve) and above. Considering larger h/b and r/R ratios when designing the hollow FRP profile will obtain a higher buckling capacity up to 2.25 times for the same b/t ratio with an increase in the cross-sectional area up to 26.5% (at h/b = 1.5 and r/R = 2). An increase of 55.8% in the cross-sectional area (twice the first value) would be needed if this buckling capacity is to be achieved by disregarding this interaction and increasing the wall thickness only.

6.2 Effect of the flange-web parameters

The contribution of each flange-web parameter on the flexural behaviour of the hollow box PFRP beam is shown in Table 8 that shows the two-way ANOVA model results. The flange-

web stiffness (calculated using the deflection of the corner's centroid) increased by 16.1% and 11.9% per 1 mm increase in the flange and web thickness, respectively. Despite the significant effect of the flange slenderness and web slenderness on the flange-web junction performance, it was found that the dominant parameter was the corner geometry (corner radii ratio). It contributed more than 60% to the flange-web stiffness and buckling strength. This was referred to the higher rigidity attained by the increased area of web-flange junction, which redistributes the stresses uniformly and alleviates stress concentration at this critical zone. Moreover, increasing the corner area reduces the unsupported length of the flange and the webs, consequently, increasing their stability. Economically, it would be better to invest in a thicker flange with thin webs to eliminate local buckling in the profile at a lower cost than manufacturing a thin flange with thick webs to transfer the failure towards the corners. The optimal design for stiff corners and stable flange would have the highest investment in the r/R ratio.

The interactive relationship between the flange slenderness and the web slenderness and corner geometry was studied to characterise its effect on the profile stability and failure mode. When monitoring the failure mode, it was noticed that reducing h/t_w and increasing r/R shifts the failure mode from local buckling of the top flange to compressive failure of the top flange and corners. The interaction between the flange slenderness and web slenderness is shown in Fig. 17 (a). The enhancement in the buckling resistance when the web thickness is increased was higher for the thin flange compared to the thicker flange. This is because of the low buckling capacity of the thin flange, which was enhanced significantly by the redistribution of stresses when the web thickness was increased. However, the failure mode shifts towards compressive failure of fibres when the flange thickness is increased. Thus, increasing the web thickness will have a lower influence on the high flexural strength of the profile as buckling is alleviated and a stable configuration is reached. This observation was also noticed for the r/R ratio effect on the flange

slenderness but on a larger scale, as shown in Fig. 17 (b), since the r/R ratio is the most influencing parameter on the flange-web junction. Flange slenderness of $b/t_f \leq 15.6$, web slenderness of $19.2 \geq h/t_w \geq 16.4$, and corner radii ratio of $r/R \geq 2$ will provide an economical configuration for the flange-web junction and obtain a stable profile that will fail at its ultimate material strength.

7. CONCLUSIONS

In this research, a numerical investigation was undertaken on the manufacturing design parameters controlling the flexural behaviour of hollow box PFRP profiles. A reliable modelling approach was established in order to obtain accurate predictions. An adjustment was performed on the incremental approach presented by the authors [16] to suit flexural loading and reduce the computational cost. A large experimental program comprising 20 beams was performed to validate this modelling approach under four-point bending. The FEM results closely agreed with experimental results and had good agreement with the theoretical result. Full factorial parametric studies were performed to obtain the effect, contribution, and interaction of the manufacturing parameters. The layup parameters (the wound fibre angle, axial-to-wound fibres ratio, and stacking sequence) were found to be insignificant compared to the geometric parameters (the wall thickness, cross-sectional aspect ratio, and the corner radius). The failure map for each geometric parameter was generated to assess its applicable levels in the factorial study. Useful guidelines on the design for manufacturing were concluded and recommended configurations of the design parameters were obtained. From this research, the following conclusions were drawn:

- Local buckling of the top flange is a critical triggering failure mode of hollow wound PFRP beams. It severely demotes the flexural strength of the profile and restrains its potentials. Under such instability condition, the flexural behaviour of these profiles is

governed by the geometric parameters of the hollow cross-section. This failure mode can be eliminated and the ultimate strength of the profile can be attained using either a wall slenderness ratio of $b/t \leq 16.4$, a cross-sectional aspect ratio of $3 > h/b \geq 1.5$, or corner radii ratio of $r/R \geq 2.5$.

- The most significant geometric parameter affecting the buckling strength of hollow PFRP profiles is the r/R ratio. Increasing it will reduce the effective buckling width of the wall, enhance the corners restraint, and increase the rigidity transferred between the walls. When compared to the wall thickness, increasing the r/R ratio obtains a higher buckling capacity at a lower cost (weight).
- From the structural design perspective, Fig. 16 represent a vital design tool, which shows the importance of the interaction between the geometric parameters on the flexural strength and failure modes of hollow PFRP profiles. Considering this interaction during the design stage will obtain more economical and enhanced design configurations up to doubled flexural strength and half cost (weight). A hollow box profile with $b/t = 21.7$, $h/b = 1.5$, and $r/R = 2$ presents the recommended configuration of the geometric parameters to shift the failure mode from local buckling to compressive failure of the top flange and obtain the ultimate material strength for flexural applications.
- The flange-web junction plays a major role in resisting buckling of top flange and webs. The top corners geometry is the main parameter controlling the rigidity, strength, and failure mode of the flange-web junction. Taking the interaction between the r/R ratio and the walls slenderness ratio into account can provide an enhanced design configuration that will fail at the ultimate material strength. This configuration was found to consist of wall slenderness ratios of $b/t_f \leq 15.6$ and $19.2 \geq h/t_w \geq 16.4$ along with a corner radii ratio of $r/R \geq 2$.

ACKNOWLEDGEMENTS

The work was funded through a Cooperative Research Centres Projects (CRC-P) Grant (CRCPSIX000117). The authors wish to thank all the supporters for their finance and providing the required computational resources and testing specimens.

APPENDIX A.

Table A. 1 shows the design of experiment of the full factorial study on the geometric parameters of the hollow box pultruded FRP beam along with its numerical results.

Table A. 1: Design matrix and results of the full factorial study on the geometric parameters of the hollow box beam (Wound fibre angle (Deg)= 50, Axial-to-wound fibre ratio (%)=[82.2/17.8], Stacking sequence=[0/+θ/-θ/0/-θ/+θ/0], R=10 mm).

Series	Wall thickness (mm)	Cross-sectional aspect ratio (h/b)	Corner radii ratio (r/R)	Flexural Stiffness (N/mm)	Flexural Strength (MPa)	Failure mode
S-1	4.6	1	0.5	544.4	289.7	Local buckling of top flange
S-2	4.6	1	1	568.5	327.7	Local buckling of top flange
S-3	4.6	1	2	656.9	383.7	Local buckling of top flange
S-4	4.6	1.25	0.5	630.1	335.2	Local buckling of top flange
S-5	4.6	1.25	1	663.3	369.1	Local buckling of top flange
S-6	4.6	1.25	2	773.3	431.5	Compressive failure of top flange
S-7	4.6	1.5	0.5	700.3	364.9	Local buckling of top flange
S-8	4.6	1.5	1	739.1	396.2	Local buckling of top flange
S-9	4.6	1.5	2	868.7	437.3	Compressive failure of top flange
S-10	5.2	1	0.5	605.3	328.2	Local buckling of top flange
S-11	5.2	1	1	632.0	379.0	Local buckling of top flange
S-12	5.2	1	2	719.5	406.7	Local buckling of top flange
S-13	5.2	1.25	0.5	705.3	391.1	Local buckling of top flange
S-14	5.2	1.25	1	737.9	409.5	Local buckling of top flange
S-15	5.2	1.25	2	847.1	433.8	Compressive failure of top flange
S-16	5.2	1.5	0.5	784.6	410.1	Local buckling of top flange
S-17	5.2	1.5	1	822.6	416.6	Local buckling of top flange
S-18	5.2	1.5	2	951.3	428.7	Compressive failure of top flange
S-19	5.8	1	0.5	665.3	409.4	Local buckling of top flange
S-20	5.8	1	1	693.2	410.2	Local buckling of top flange
S-21	5.8	1	2	779.1	437.1	Compressive failure of top flange
S-22	5.8	1.25	0.5	778.1	407.6	Local buckling of top flange
S-23	5.8	1.25	1	809.9	411.4	Local buckling of top flange
S-24	5.8	1.25	2	917.1	437.1	Compressive failure of top flange
S-25	5.8	1.5	0.5	865.9	412.9	Local buckling of top flange
S-26	5.8	1.5	1	903.2	414.9	Local buckling of top flange
S-27	5.8	1.5	2	1029.7	426.9	Compressive failure of top flange

Table A. 2 shows the design of experiment of the full factorial study on the flange-web parameters of the hollow box pultruded FRP beam along with its numerical results. The flange-web stiffness was calculated using the deflection of the corner's centroid.

Table A. 2. Design matrix and results of the full factorial study on the flange-web parameters of the hollow box beam (Wound fibre angle (Deg)= 50, Axial-to-wound fibre ratio (%)=[82.2/17.8], Stacking sequence=[0/+θ/-θ/0/-θ/+θ/0], R=10 mm, h/b=1).

Series	Flange thickness (mm)	Web thickness (mm)	Corner radii ratio (r/R)	Flange-web Stiffness (N/mm)	Flexural Strength (MPa)	Failure mode
S-1	4.6	4.6	0.5	544.4	290.7	Local buckling of top flange and webs
S-2	4.6	4.6	1	568.1	324.7	Local buckling of top flange and webs
S-3	4.6	4.6	2	659.3	383.3	Compressive failure of top corners
S-4	4.6	5.2	0.5	564.2	317.1	Local buckling of top flange and webs
S-5	4.6	5.2	1	591.8	342.9	Local buckling of top flange and webs
S-6	4.6	5.2	2	683.9	400.1	Compressive failure of top corners
S-7	4.6	5.8	0.5	587.2	334.4	Local buckling of top flange and webs
S-8	4.6	5.8	1	614.9	360.4	Local buckling of top flange and webs
S-9	4.6	5.8	2	707.8	426.5	Compressive failure of top corners
S-10	5.2	4.6	0.5	581.1	320.8	Local buckling of top flange and webs
S-11	5.2	4.6	1	607.9	345.3	Local buckling of top flange and webs
S-12	5.2	4.6	2	696.5	396.2	Compressive failure of top corners
S-13	5.2	5.2	0.5	605.3	328.2	Local buckling of top flange and webs
S-14	5.2	5.2	1	632.0	373.5	Local buckling of top flange and webs
S-15	5.2	5.2	2	719.5	397.0	Compressive failure of top corners
S-16	5.2	5.8	0.5	627.6	366.7	Local buckling of top flange and webs
S-17	5.2	5.8	1	654.6	391.9	Local buckling of top flange and corners failure
S-18	5.2	5.8	2	744.8	418.3	Compressive failure of top flange and corners
S-19	5.8	4.6	0.5	620.2	351.4	Local buckling of top flange and webs
S-20	5.8	4.6	1	646.7	377.9	Compressive failure of top flange and corners
S-21	5.8	4.6	2	732.6	401.4	Compressive failure of top corners
S-22	5.8	5.2	0.5	643.8	369.3	Local buckling of top flange and webs
S-23	5.8	5.2	1	670.0	393.8	Compressive failure of top flange and corners
S-24	5.8	5.2	2	757.1	410.9	Compressive failure of top corners
S-25	5.8	5.8	0.5	665.3	385.5	Local buckling of top flange and webs
S-26	5.8	5.8	1	692.9	400.1	Compressive failure of top flange and corners
S-27	5.8	5.8	2	780.6	413.2	Compressive failure of top corners

REFERENCES

[1] Gand AK, Chan T-M, Mottram JT. Civil and structural engineering applications, recent trends, research and developments on pultruded fiber reinforced polymer closed sections: a review. Front Struct Civ Eng 2013;7:227–44. https://doi.org/10.1007/s11709-013-0216-8.

[2] Vedernikov A, Safonov A, Tucci F, Carlone P, Akhatov I. Pultruded materials and structures: A review. J Compos Mater 2020;54:4081–117. https://doi.org/10.1177/0021998320922894.

[3] Al-saadi AU, Aravinthan T, Lokuge W. Effects of fibre orientation and layup on the mechanical properties of the pultruded glass fibre reinforced polymer tubes. Eng Struct 2019;198:109448. https://doi.org/10.1016/j.engstruct.2019.109448.

[4] Hizam RM, Manalo AC, Karunasena W, Bai Y. Behaviour of pultruded GFRP truss system connected using through-bolt with mechanical insert. Compos Part B Eng 2019;168:44–57. https://doi.org/10.1016/j.compositesb.2018.12.052.

[5] Muttashar M, Karunasena W, Manalo A, Lokuge W. Behaviour of hollow pultruded GFRP square beams with different shear span-to-depth ratios. J Compos Mater 2016;50:2925–40. https://doi.org/10.1177/0021998315614993.

[6] Sayyad AS, Ghugal YM. Bending, buckling and free vibration of laminated composite and sandwich beams: A critical review of literature. Compos Struct 2017;171:486–504. https://doi.org/10.1016/j.compstruct.2017.03.053.

[7] Awad ZK, Aravinthan T, Zhuge Y, Gonzalez F. A review of optimization techniques used in the design of fibre composite structures for civil engineering applications. Mater Des 2012;33:534–44. https://doi.org/10.1016/j.matdes.2011.04.061.

[8] Correia JR, Branco FA, Silva NMF, Camotim D, Silvestre N. First-order, buckling and post-buckling behaviour of GFRP pultruded beams. Part 1: Experimental study. Comput Struct 2011;89:2052–64. https://doi.org/10.1016/j.compstruc.2011.07.005.

[9] Department of Defense. Composite materials handbook, volume 3: polymer matrix composites—materials usage, design and analysis. SAE International; 2002.

[10] Uddin N. Developments in Fiber-Reinforced Polymer (FRP) Composites for Civil Engineering. Elsevier; 2013.

[11] Xu J, Zhao Q, Qiao P. A critical review on buckling and post-buckling analysis of composite structures. Front Aerosp Eng 2013;2:157–68.

[12] American Society of Civil Engineers. Pre-standard for load & resistance factor design (LRFD) of pultruded fiber reinforced polymer (FRP) structures. Arlingt VA ACMA 2012:215.

[13] Ascione L, Caron J-F, Godonou P, van Ijselmuijden K, Knippers J, Mottram T, et al. Prospect for new guidance in the design of FRP : Support to the implementation, harmonization and further development of the Eurocodes. Publications Office of the European Union; 2016.

[14] Bank LC. Composites for Construction: Structural Design with FRP Materials. John Wiley & Sons; 2006.

[15] Kollár LP, Springer GS. Mechanics of Composite Structures. Cambridge University Press; 2003.

[16] Alhawamdeh M, Alajarmeh O, Aravinthan T, Shelley T, Schubel P, Kemp M, et al. Modelling hollow pultruded FRP profiles under axial compression: Local buckling and progressive failure. Compos Struct 2021;262:113650. https://doi.org/10.1016/j.compstruct.2021.113650.

[17] Kalantari M, Dong C, Davies IJ. Effect of matrix voids, fibre misalignment and thickness variation on multi-objective robust optimization of carbon/glass fibre-reinforced hybrid composites under flexural loading. Compos Part B Eng 2017;123:136–47. https://doi.org/10.1016/j.compositesb.2017.05.022.
[18] Nikbakt S, Kamarian S, Shakeri M. A review on optimization of composite structures Part I: Laminated composites. Compos Struct 2018;195:158–85. https://doi.org/10.1016/j.compstruct.2018.03.063.
[19] Betts D, Sadeghian P, Fam A. Investigation of the stress-strain constitutive behavior of ±55° filament wound GFRP pipes in compression and tension. Compos Part B Eng 2019;172:243–52. https://doi.org/10.1016/j.compositesb.2019.05.077.
[20] Akbaş ŞD. Post-buckling analysis of a fiber reinforced composite beam with crack. Eng Fract Mech 2019;212:70–80. https://doi.org/10.1016/j.engfracmech.2019.03.007.
[21] Asadi A, Sheikh AH, Thomsen OT. Buckling behaviour of thin-walled laminated composite beams having open and closed sections subjected to axial and end moment loading. Thin-Walled Struct 2019;141:85–96. https://doi.org/10.1016/j.tws.2019.04.005.
[22] Nguyen N-D, Nguyen T-K, Vo TP, Nguyen T-N, Lee S. Vibration and buckling behaviours of thin-walled composite and functionally graded sandwich I-beams. Compos Part B Eng 2019;166:414–27. https://doi.org/10.1016/j.compositesb.2019.02.033.
[23] Garrido M, Madeira JFA, Proença M, Correia JR. Multi-objective optimization of pultruded composite sandwich panels for building floor rehabilitation. Constr Build Mater 2019;198:465–78.
[24] Srinivasa CV, Kumar WPP, Kumar MTP, Bangar AR, Kumar P, Rudresh MS. Experimental and numerical studies on buckling of laminated composite skew plates with circular holes under uniaxial compression. Mech Adv Mater Struct 2017;24:304–17. https://doi.org/10.1080/15376494.2016.1142023.
[25] Wagner HNR, Köke H, Dähne S, Niemann S, Hühne C, Khakimova R. Decision tree-based machine learning to optimize the laminate stacking of composite cylinders for maximum buckling load and minimum imperfection sensitivity. Compos Struct 2019;220:45–63. https://doi.org/10.1016/j.compstruct.2019.02.103.
[26] Schreiber P, Mittelstedt C. A holistic approach for local buckling of composite laminated beams under compressive load. Arch Appl Mech 2019;89:1243–57. https://doi.org/10.1007/s00419-018-1496-1.
[27] Ascione L, Berardi VP, Giordano A, Spadea S. Macro-scale analysis of local and global buckling behavior of T and C composite sections. Mech Res Commun 2014;58:105–11. https://doi.org/10.1016/j.mechrescom.2013.10.004.
[28] Liu T, Vieira JD, Harries KA. Predicting Flange Local Buckling Capacity of Pultruded GFRP I-Sections Subject to Flexure. J Compos Constr 2020;24:04020025. https://doi.org/10.1061/(ASCE)CC.1943-5614.0001032.
[29] Cardoso DCT, Harries KA, Batista E de M. Closed-form equations for compressive local buckling of pultruded thin-walled sections. Thin-Walled Struct 2014;79:16–22. https://doi.org/10.1016/j.tws.2014.01.013.
[30] Tang J, Chen X, Yang K. Evaluating Structural Failure of Load-Carrying Composite Box Beams with Different Geometries and Load Conditions. Appl Compos Mater 2019;26:1151–61. https://doi.org/10.1007/s10443-019-09776-4.
[31] Bai Y, Keller T, Wu C. Pre-buckling and post-buckling failure at web-flange junction of pultruded GFRP beams. Mater Struct 2013;46:1143–54. https://doi.org/10.1617/s11527-012-9960-9.
[32] Liu T, Harries KA. Flange local buckling of pultruded GFRP box beams. Compos Struct 2018;189:463–72. https://doi.org/10.1016/j.compstruct.2018.01.101.

[33] Mosallam AS, Feo L, Elsadek A, Pul S, Penna R. Structural evaluation of axial and rotational flexibility and strength of web–flange junctions of open-web pultruded composites. Compos Part B Eng 2014;66:311–27. https://doi.org/10.1016/j.compositesb.2014.05.018.
[34] Bank LC, Gentry TR, Nadipelli M. Local Buckling of Pultruded FRP Beams-Analysis and Design. J Reinf Plast Compos 1996;15:283–94. https://doi.org/10.1177/073168449601500304.
[35] Aleksendric D, Carlone P. Soft Computing in the Design and Manufacturing of Composite Materials: Applications to Brake Friction and Thermoset Matrix Composites. Woodhead Publishing; 2015.
[36] Attaf B. Advances in Composite Materials: Ecodesign and Analysis. BoD – Books on Demand; 2011.
[37] Barbero EJ. Introduction to Composite Materials Design. CRC Press; 2017. https://doi.org/10.1201/9781315296494.
[38] Buragohain MK. Composite Structures: Design, Mechanics, Analysis, Manufacturing, and Testing. CRC Press; 2017.
[39] Gibson RF. Principles of Composite Material Mechanics. CRC Press; 2016.
[40] Mallick PK. Fiber-reinforced composites: materials, manufacturing, and design. CRC press; 2007.
[41] Matthews FL, Davies GAO, Hitchings D, Soutis C. Finite Element Modelling of Composite Materials and Structures. Elsevier; 2000.
[42] Najafi A, Rais-Rohani M. Concurrent Process-Product Design Optimization Using Coupled Nonlinear Finite-Element Simulations. Finite Elem Anal - Appl Mech Eng 2012. https://doi.org/10.5772/47852.
[43] Rammerstorfer FG. ENGINEERING MECHANICS OF FIBRE REINFORCED POLYMERSAND COMPOSITE STRUCTURES. Springer; 1994.
[44] Soares CAM, Soares CMM, Freitas MJM. Mechanics of Composite Materials and Structures. Springer Science & Business Media; 2013.
[45] Vasiliev VV, Morozov EV. Advanced Mechanics of Composite Materials and Structures. Elsevier; 2018.
[46] Abouzied A, Masmoudi R. Flexural behavior of rectangular FRP-tubes filled with reinforced concrete: Experimental and theoretical studies. Eng Struct 2017;133:59–73. https://doi.org/10.1016/j.engstruct.2016.12.010.
[47] ASTM D7249/D7249M. Standard test method for facing properties of sandwich constructions by long beam flexure. Am Soc Test Mater 2012.
[48] Cole B, Fam A. Flexural Load Testing of Concrete-Filled FRP Tubes with Longitudinal Steel and FRP Rebar. J Compos Constr 2006;10:161–71. https://doi.org/10.1061/(ASCE)1090-0268(2006)10:2(161).
[49] Muttashar M, Manalo A, Karunasena W, Lokuge W. Influence of infill concrete strength on the flexural behaviour of pultruded GFRP square beams. Compos Struct 2016;145:58–67. https://doi.org/10.1016/j.compstruct.2016.02.071.
[50] Simulia DS. Abaqus 6.13 Analysis User's Guide. Dassault Syst Provid RI 2013.
[51] Al-Saadi A, Aravinthan T, Lokuge W. Numerical Investigation on Hollow Pultruded Fibre Reinforced Polymer Tube Columns. ACMSM25, Springer; 2020, p. 455–65.
[52] Daniel IM, Ishai O. Engineering Mechanics of Composite Materials. Oxford University Press; 2006.
[53] Sharma AP, Khan SH, Parameswaran V. Experimental and numerical investigation on the uni-axial tensile response and failure of fiber metal laminates. Compos Part B Eng 2017;125:259–74. https://doi.org/10.1016/j.compositesb.2017.05.072.

[54] Regel F. A modelling approach for 3D braid reinforced composites under non-axial loading. PhD Thesis. University of Minho, 2014.
[55] Antony J. Design of Experiments for Engineers and Scientists. 2nd Edition. Elsevier; 2014.
[56] Reddy JN. Mechanics of Laminated Composite Plates and Shells: Theory and Analysis, Second Edition. CRC Press; 2003.
[57] Wagners CFT. Wagners-Composite Fibre Technologies (CFT). Wagner n.d. https://www.wagner.com.au/main/what-we-do/composite-fibre-technologies/cft-home/ (accessed March 8, 2020).
[58] Clarke JL. Structural Design of Polymer Composites EUROCOMP Design Code and Handbook. CRC Press; 2005.
[59] Godat A, Légeron F, Gagné V, Marmion B. Use of FRP pultruded members for electricity transmission towers. Compos Struct 2013;105:408–21. https://doi.org/10.1016/j.compstruct.2013.05.025.
[60] Meyer R. Handbook of Pultrusion Technology. Springer Science & Business Media; 2012.
[61] Starr T. Pultrusion for Engineers. Elsevier; 2000.
[62] Minitab-18. Minitab Reference Manual: statistical software. Minitab Inc. State College, PA; 2017.
[63] Estep DD, GangaRao HVS, Dittenber DB, Qureshi MA. Response of pultruded glass composite box beams under bending and shear. Compos Part B Eng 2016;88:150–61. https://doi.org/10.1016/j.compositesb.2015.11.008.
[64] Quadrino A, Penna R, Feo L, Nisticò N. Mechanical characterization of pultruded elements: Fiber orientation influence vs web-flange junction local problem. Experimental and numerical tests. Compos Part B Eng 2018;142:68–84. https://doi.org/10.1016/j.compositesb.2018.01.001.

FIGURES

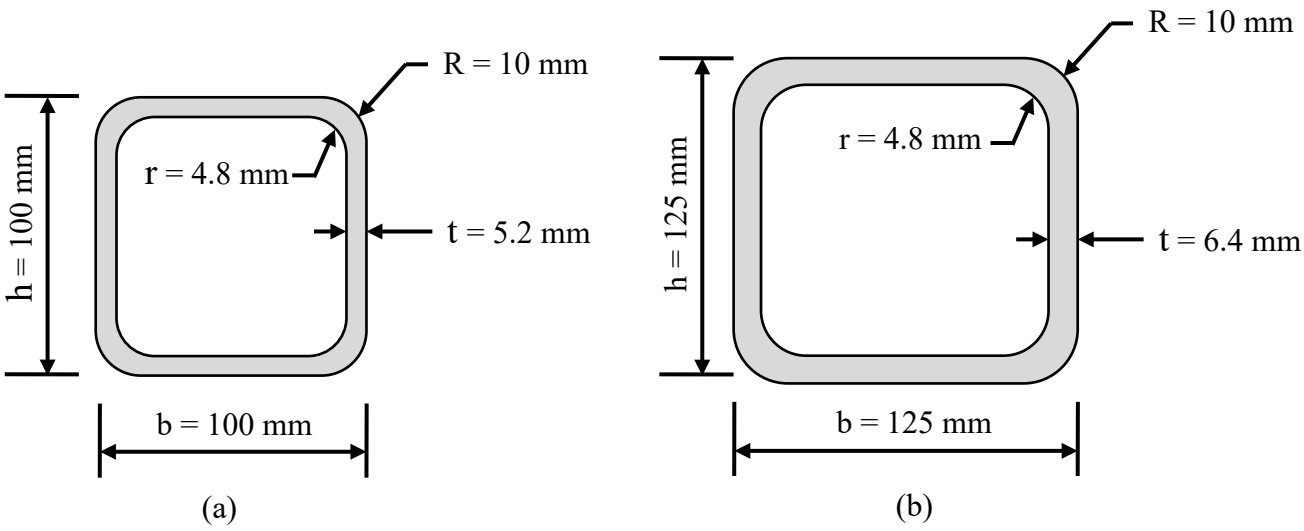

Fig. 1. Cross-sectional dimensions of (a) S-100×100×5.2 and (b) S-125×125×6.4 hollow box PFRP profiles.

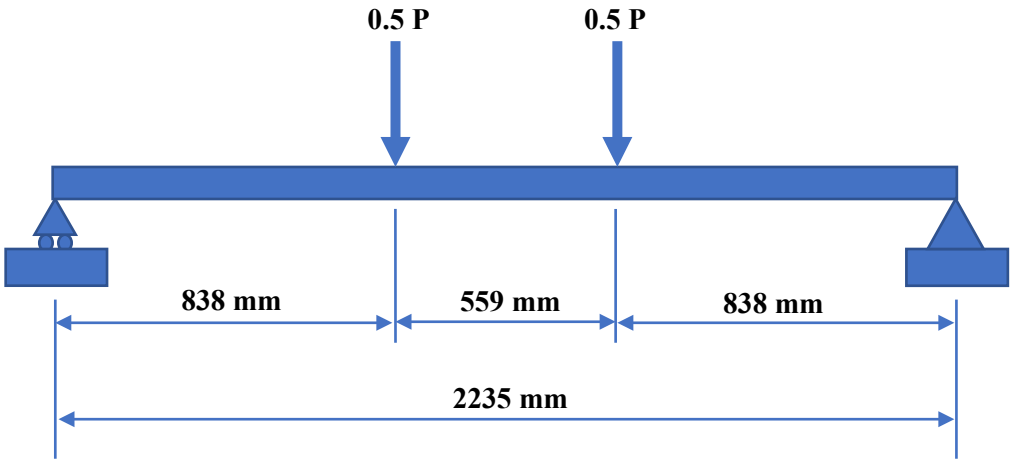

Fig. 2. Four-point bending test configuration and dimensions of a simply supported beam.

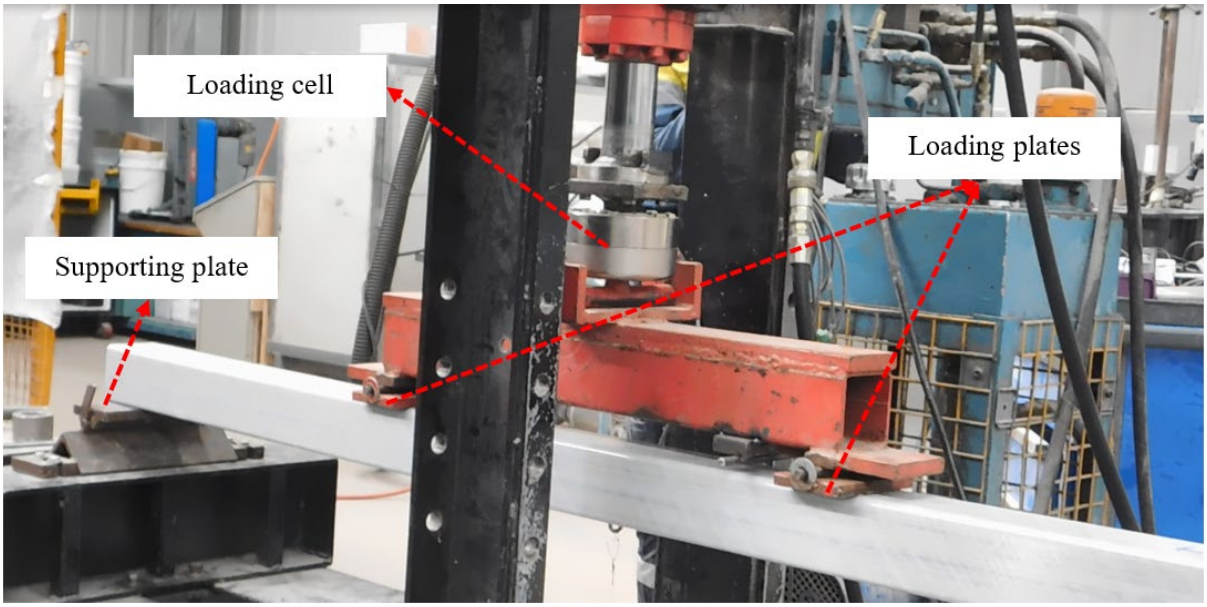

Fig. 3. Hollow box PFRP profile loaded under four-point bending test configuration.

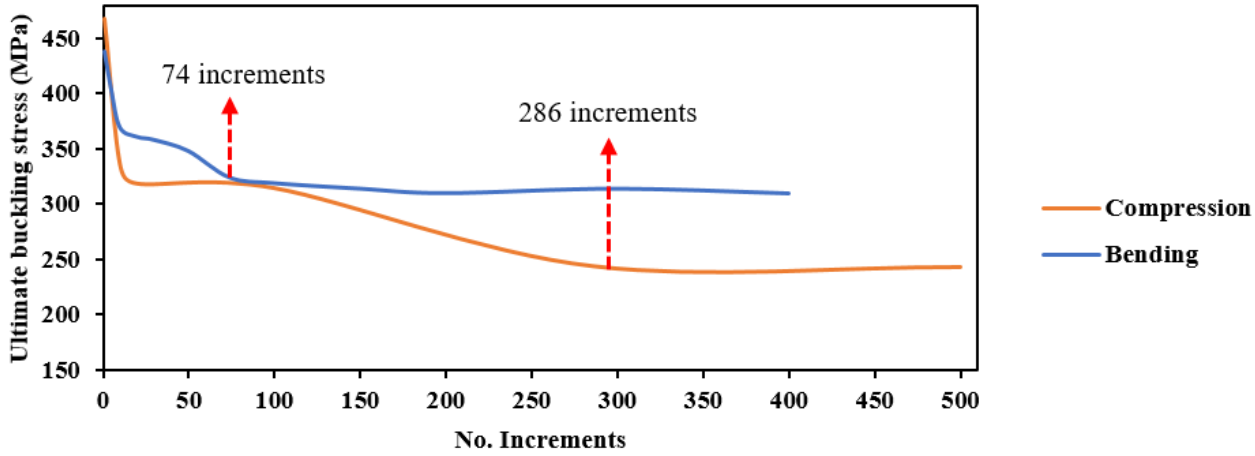

Fig. 4. Ultimate buckling stress convergence when reducing the increment size for the S-100×100×5.2 profile under compression [16] and bending (current study).

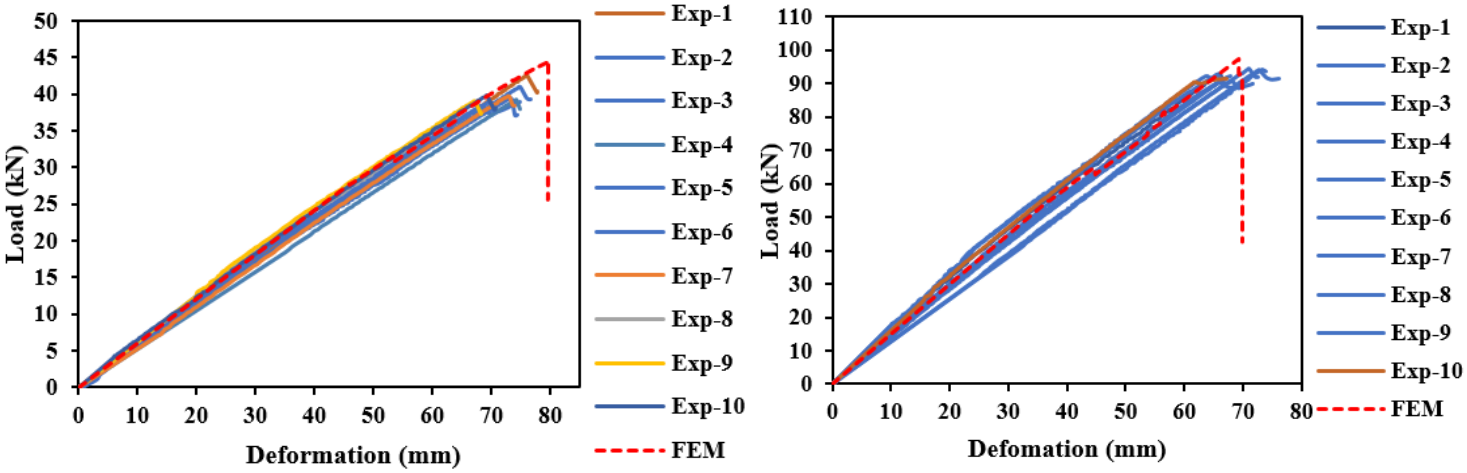

Fig. 5. FEM vs experimental load-deflection curves of (a) S-100×100×5.2 and (b) S-125×125×6.4 beams.

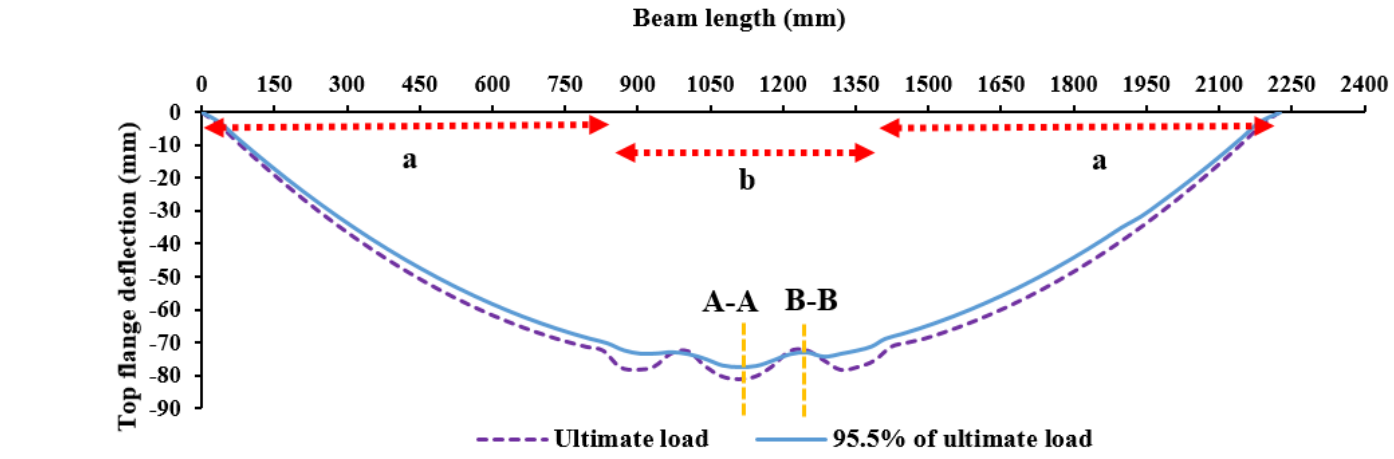

(a)

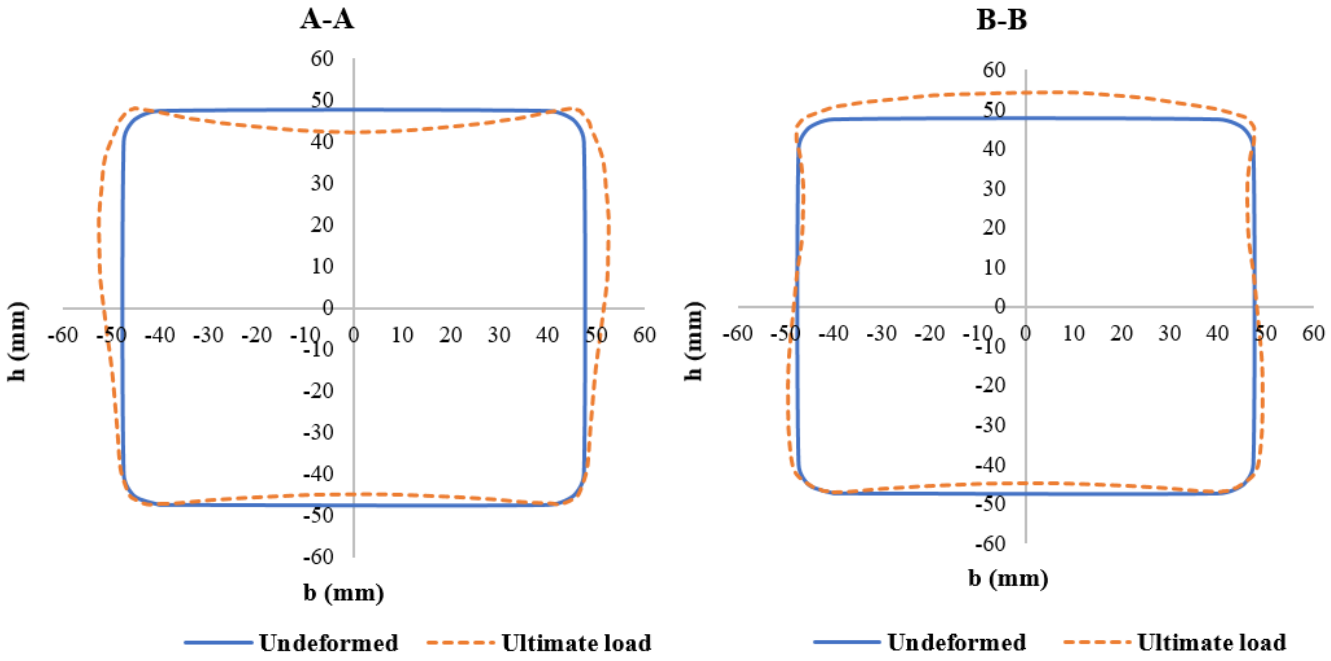

(b)

(c)

Fig. 6. Numerical visualisation showing (a) the deflected shape of the top flange of S-100×100×5.2 beam and the cross-sections of S-100×100×5.2 beam at the ultimate load point (b) cross-section A-A and (c) cross-section B-B.

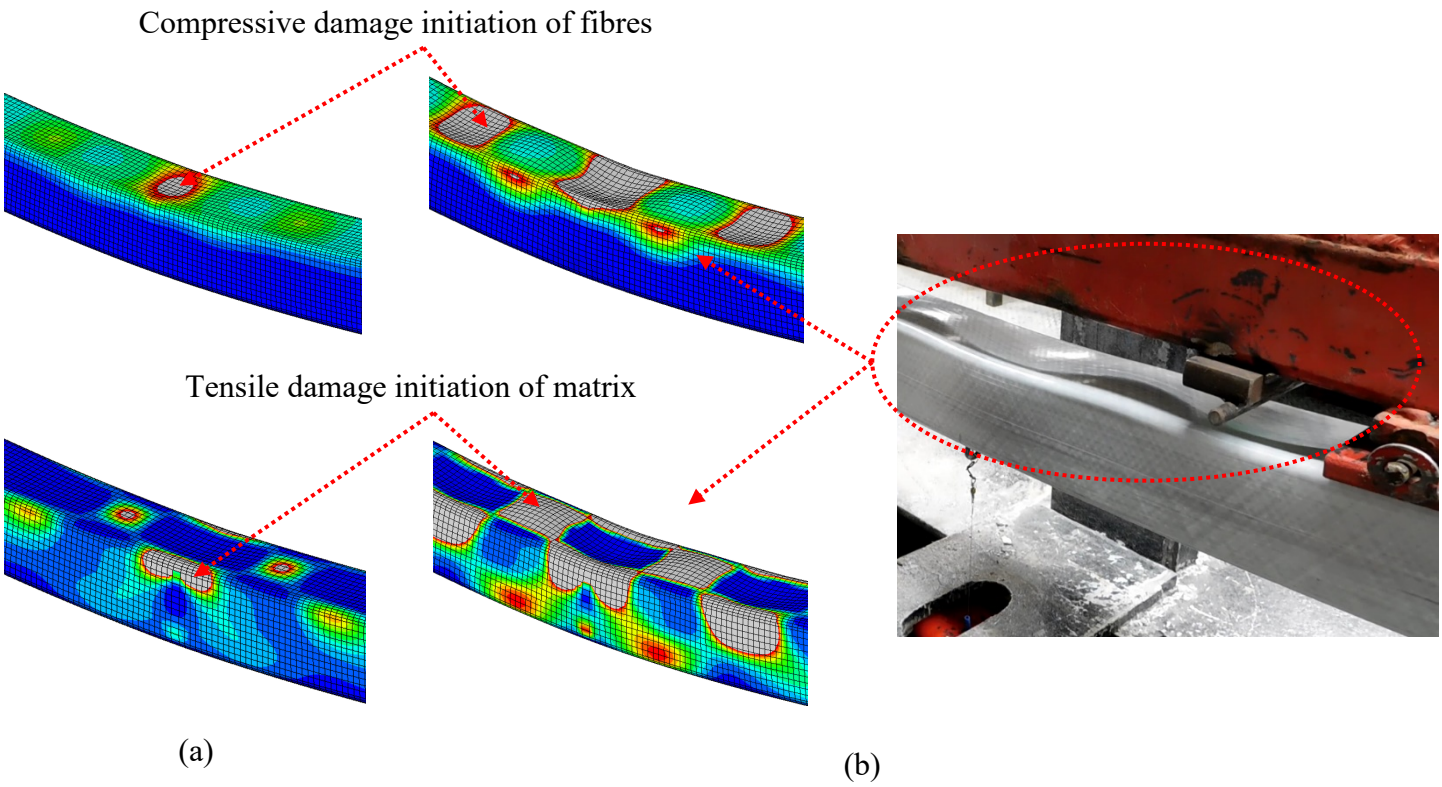

Fig. 7. Failure sequence of S-100×100×5.2 beam starting by local buckling of the top flange at (a) 95.5% of ultimate load followed by localised waviness propagation until (b) the ultimate load point.

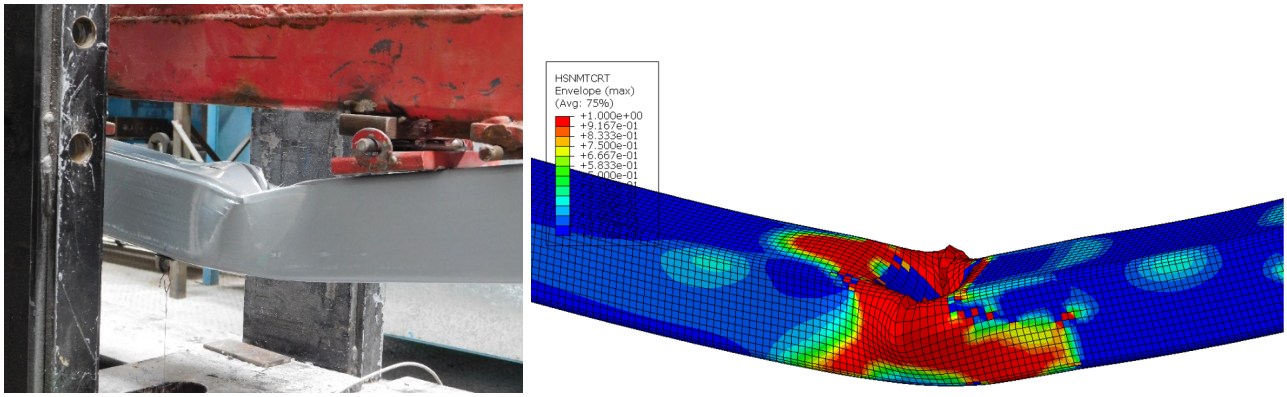

(a)

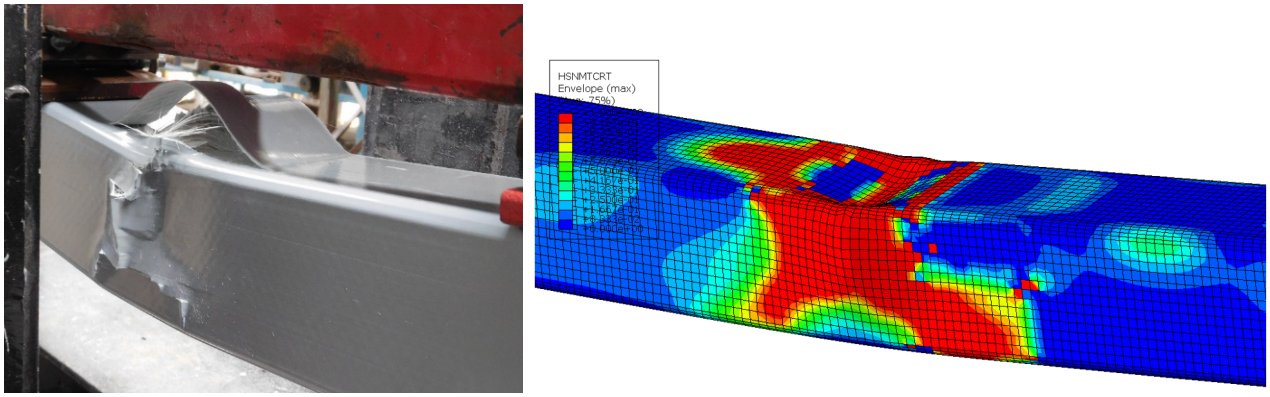

(b)

Fig. 8. Experimental vs numerical collapse of (a) S-100×100×5.2 and (b) S-125×125×6.4 beams.

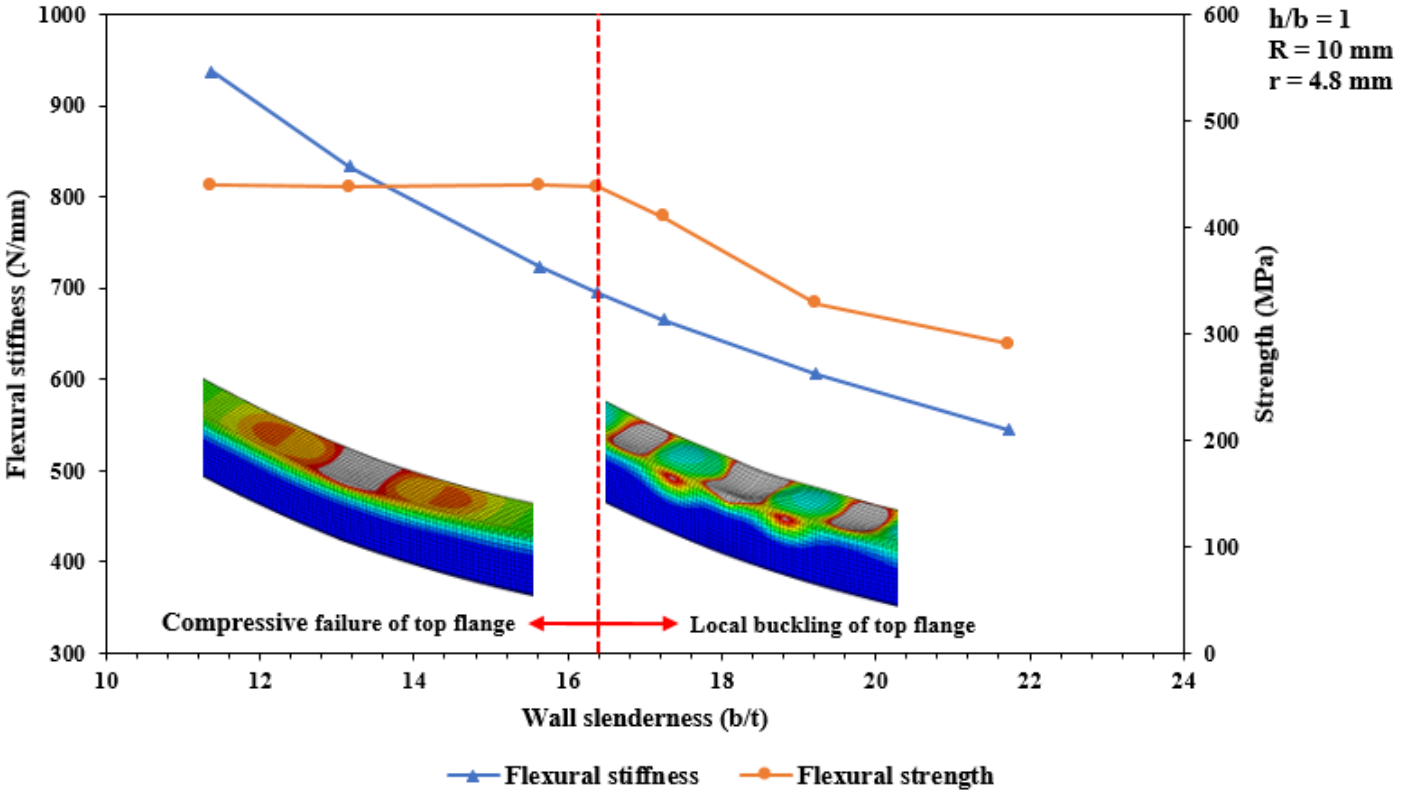

Fig. 9. Wall thickness effect on the flexural behaviour of hollow box PFRP profile.

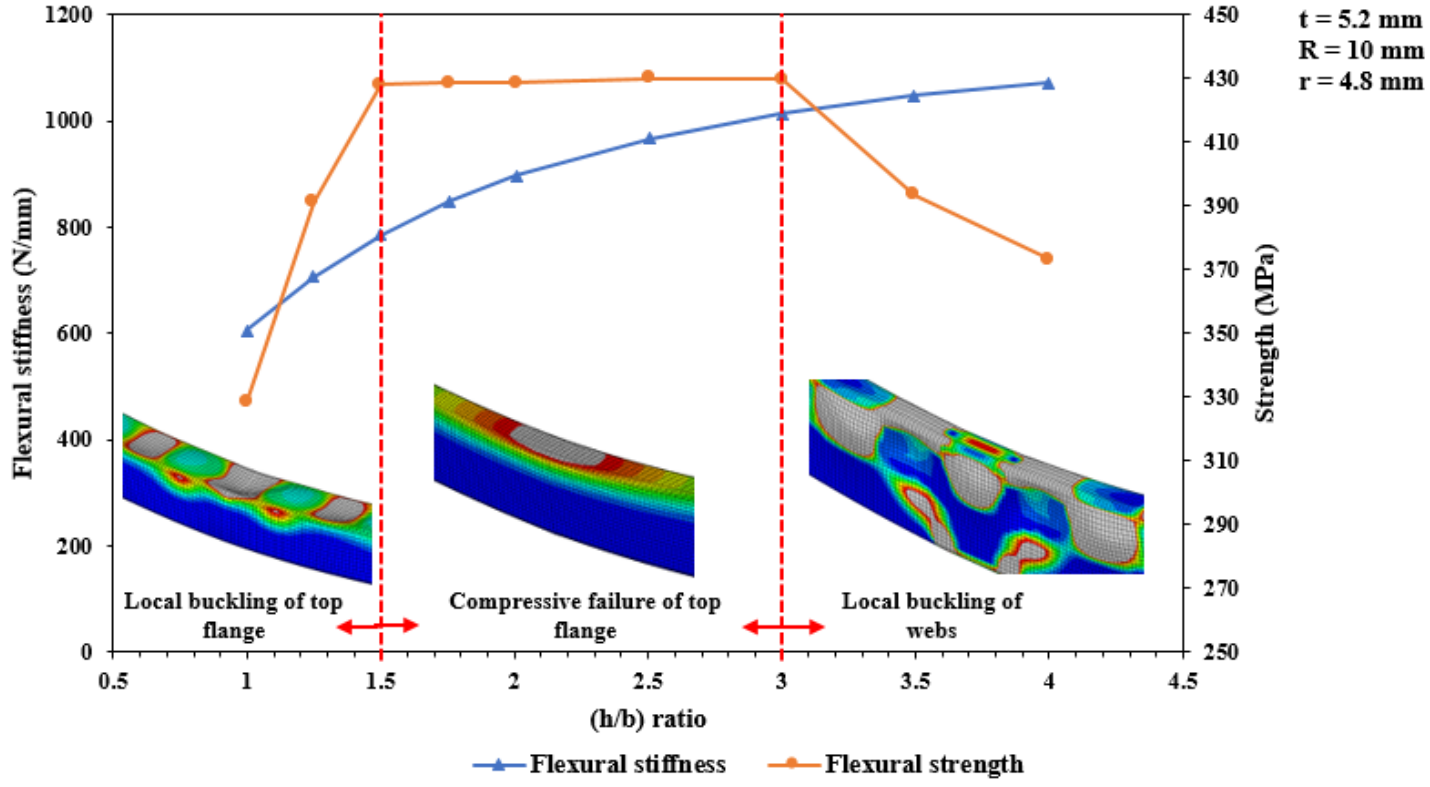

Fig. 10. Effect of the cross-sectional aspect ratio on the flexural behaviour of hollow box pultruded FRP beam.

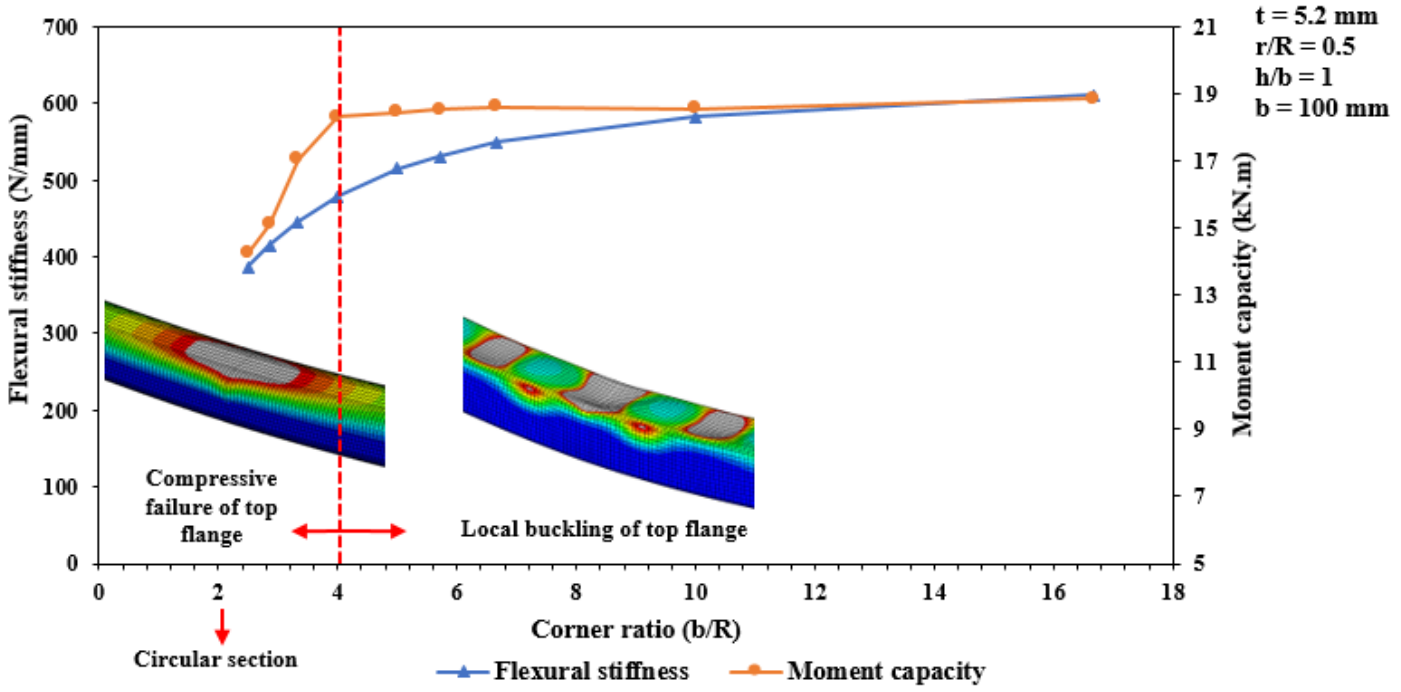

Fig. 11. Outer corner radius effect on the flexural behaviour of hollow box pultruded FRP beam.

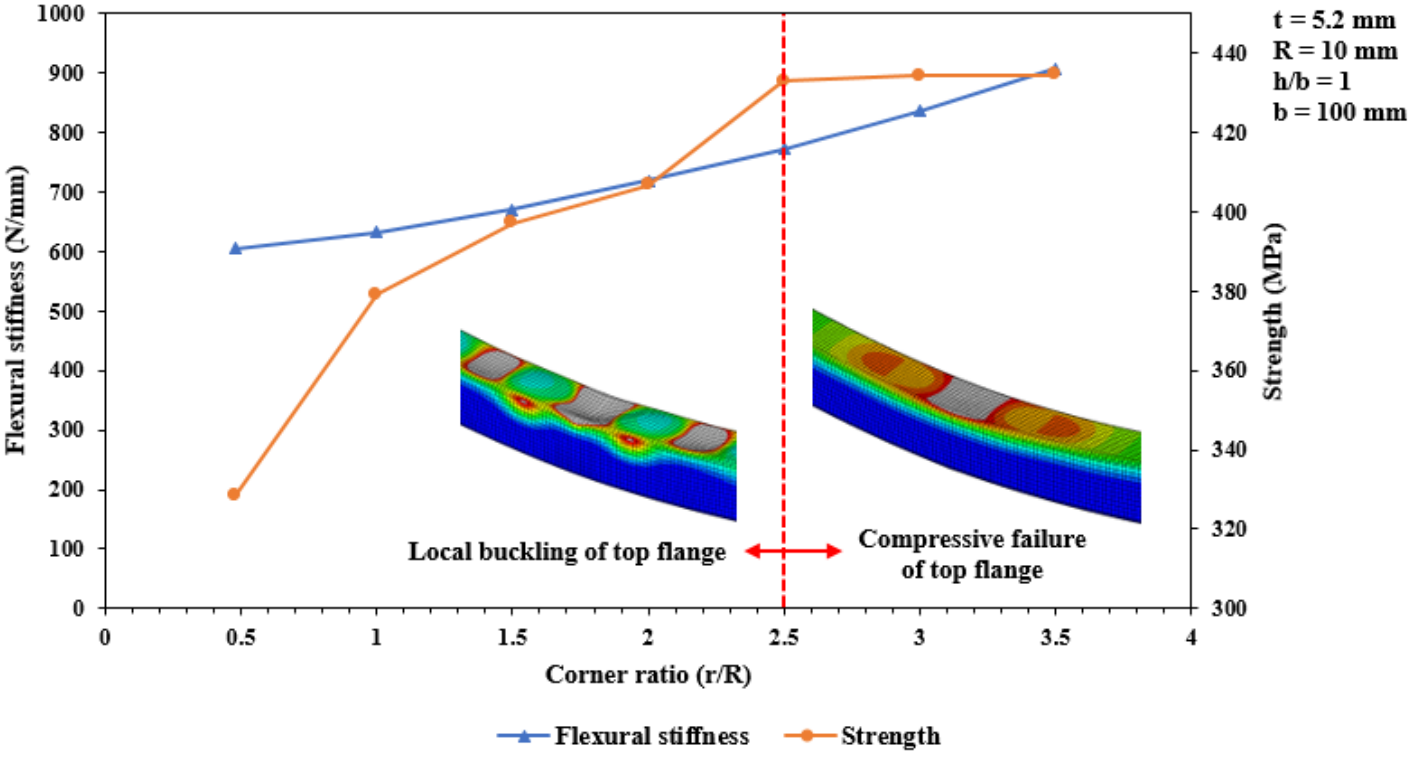

Fig. 12. Effect of the corner inner-to-outer radii ratio (r/R) on the flexural behaviour of hollow box PFRP beam.

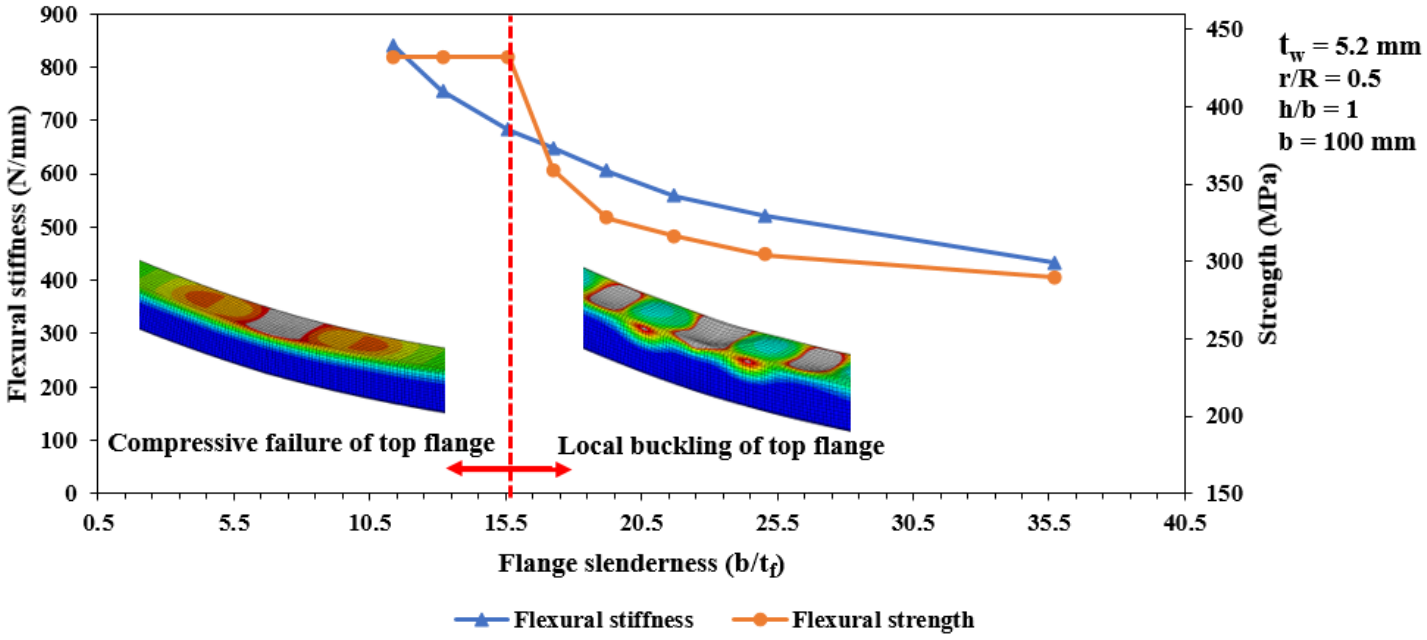

Fig. 13. Flange slenderness effect on the flexural behaviour of hollow box PFRP profile.

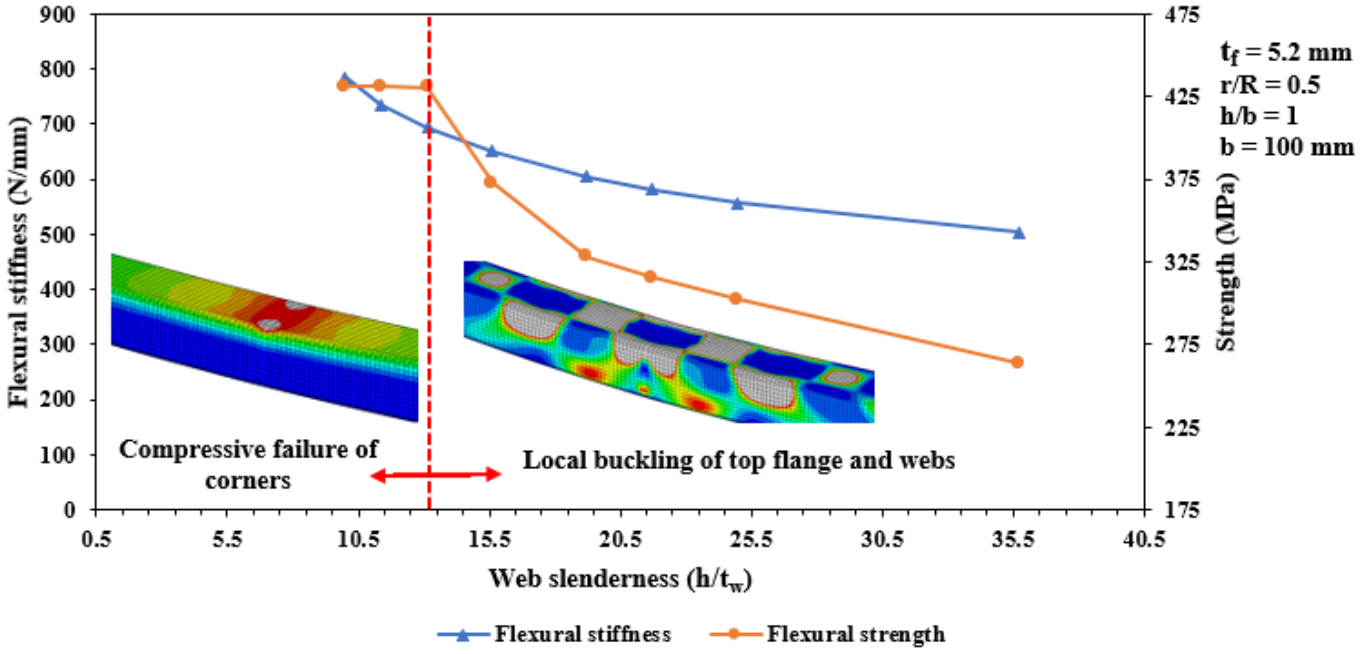

Fig. 14. Web slenderness effect on the flexural behaviour of hollow box PFRP profile.

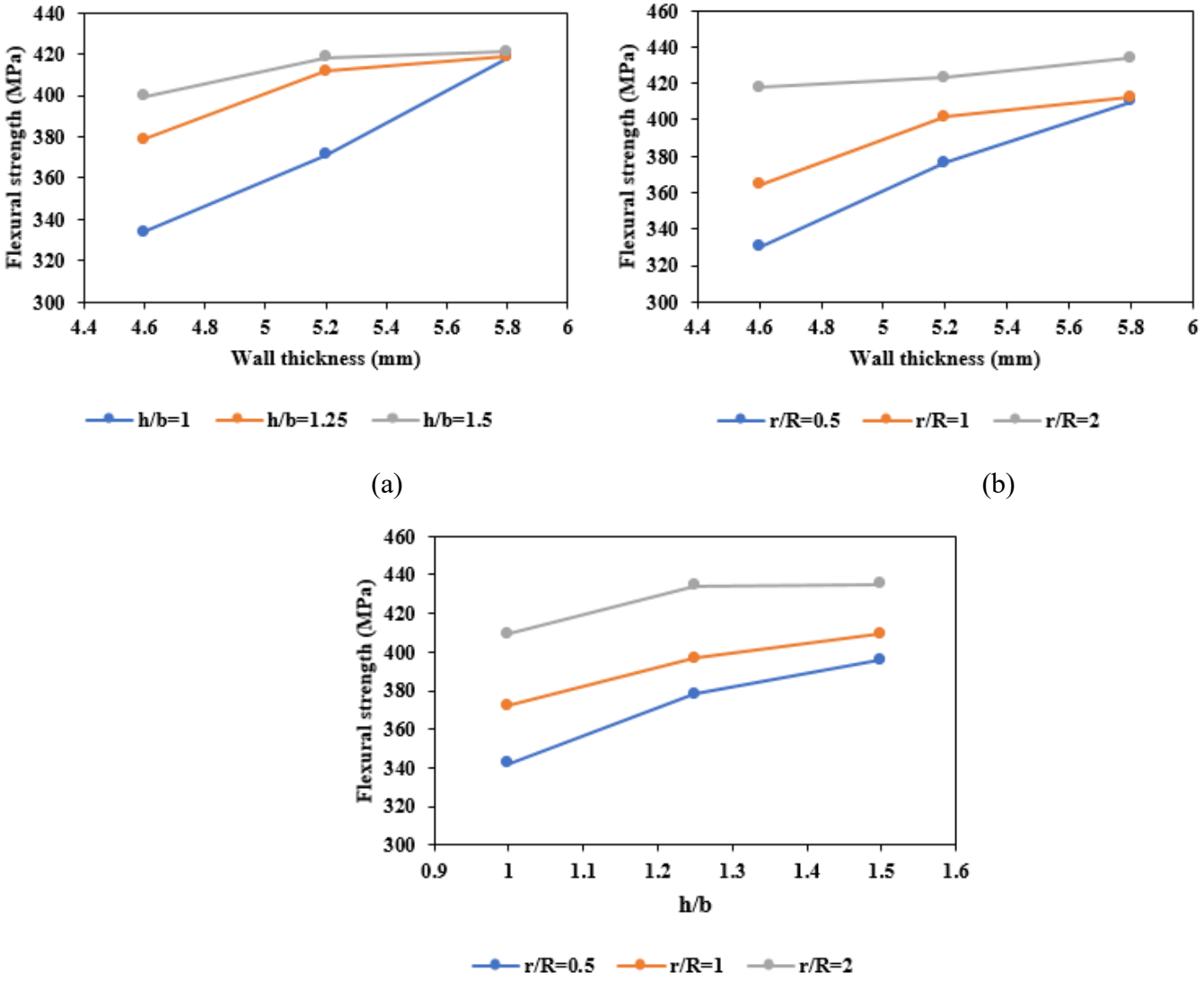

Fig. 15. Interaction plots of the geometric parameters affecting the flexural strength of hollow box PFRP beam (a) wall thickness and h/b ratio (b) wall thickness and corner radius and (c) h/b ratio and corner radius.

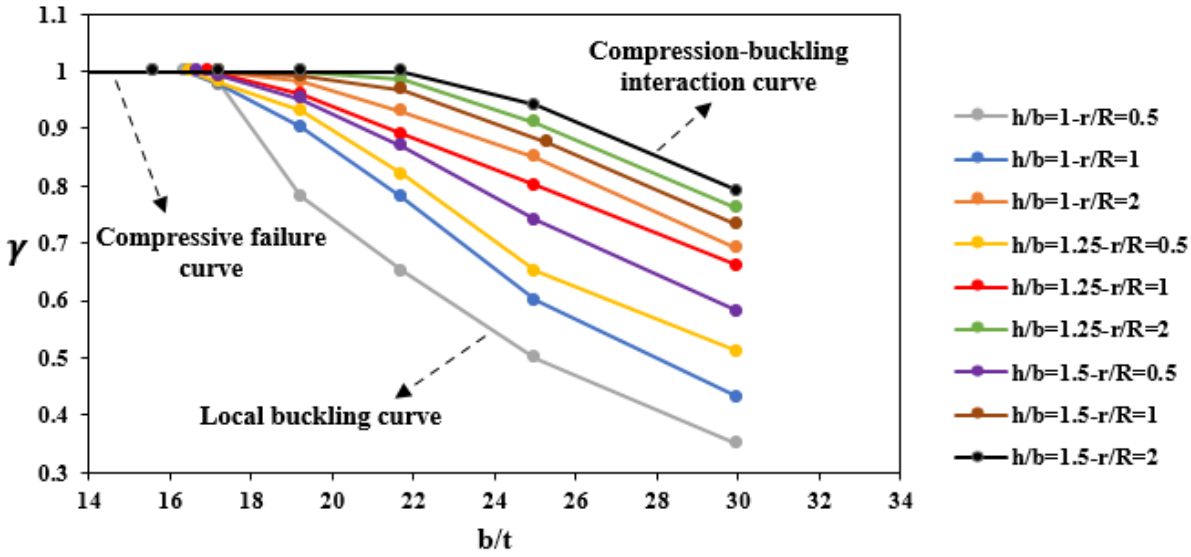

Fig. 16. Interaction plot of failure modes controlling the flexural behaviour of hollow box PFRP beam.

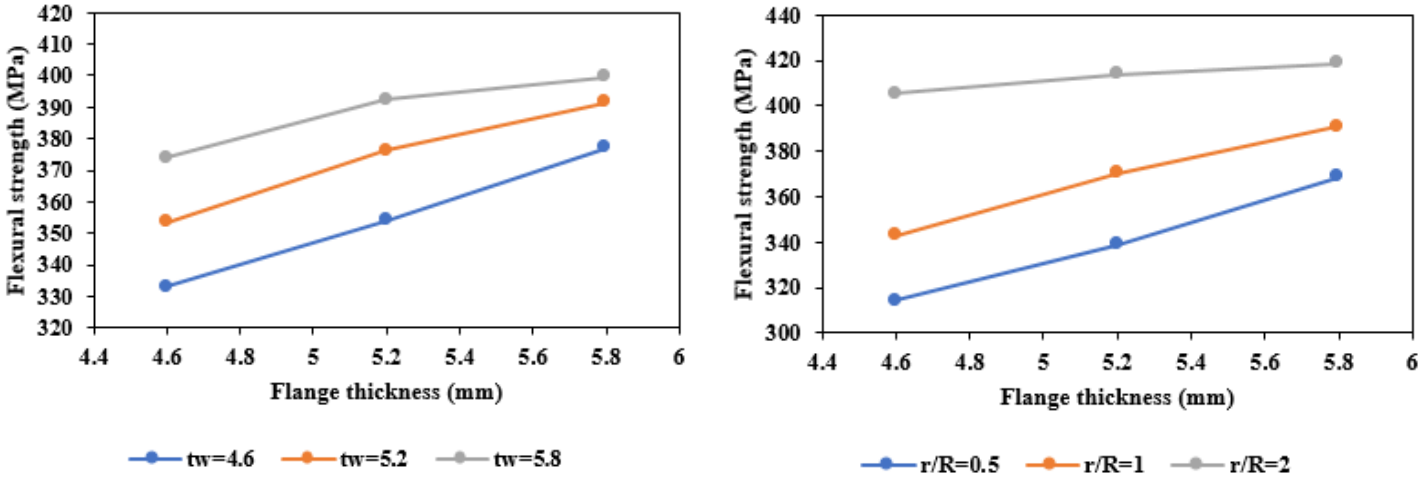

(a) (b)

Fig. 17. Interaction plots of the flange-web parameters affecting the flexural strength of hollow box PFRP beam (a) flange thickness and web thickness and (b) flange thickness and corner radius.

TABLES

Table 1: Layup and geometric properties of hollow PFRP profiles.

Profile label		S-100×100×5.2	S-125×125×6.4
Geometric properties	Wall width (mm)	100	125
	Wall thickness (mm)	5.2	6.4
	Outer corner radius (mm)	10	10
	Inner corner radius (mm)	4.8	4.8
Layup properties	Stacking sequence	[0/+50/-50/0/-50/+50/0]	[0/+50/0/-50/0/-50/0/+50/0]
	Fibre percentage (%)	0^o: 82.2, 50^o: 17.8	0^o: 78.1, 50^o: 21.9

Table 2: lamina mechanical properties of the hollow box pultruded FRP profiles.

Elastic properties		Strength limits		Fracture energy	
E_1(MPa)	45700	X^T (MPa)	803	G_{LT} (N/mm)	92
E_2(MPa)	12100	X^C (MPa)	548	G_{LC} (N/mm)	79
v_{12}	0.28	Y^T (MPa)	43	G_{TT} (N/mm)	5
$G_{12} = G_{13}$ (MPa)	4600	Y^C (MPa)	187	G_{TC} (N/mm)	5
G_{23}(MPa)	4000	S^L (MPa)	64		
		S^T (MPa)	50		

Table 3: Comparison of the probable failure modes and the current study results.

Result source	Failure mode	S-100×100×5.2	S-125×125×6.4
Theoretical	Local Buckling of Walls Due to In-Plane Compression (kN) [12,14,15,37]	30.15	58.27
	Local Buckling of Walls Due to In-Plane Shear (kN) [12,14,15,37]	75.63	119.01
	Web Crushing in the Transverse Direction (kN) [12,14]	224.81	273.61
	Web Buckling in the Transverse Direction (kN) [12,14]	359.62	395.33
	Flange and Web Longitudinal Material Failure (kN) [14,37]	64.82	127.60
	Flange and Web Material Shear Failure (kN) [14,37]	64.73	109.89
Experimental	Average experimental ultimate load (kN)	40.12	92.13
Numerical	FEM ultimate load (kN)	44.65	97.27

Table 4: Theoretical vs experimental and FEM local buckling loads of hollow box PFRP beams.

Reference	Buckling stress $(\sigma)_{cr}$ Equation	Profile					
		S-100×100×5.2			S-125×125×6.4		
		$(\sigma)_{cr}$ (MPa)	$(\sigma_{cr})_{EXP}$ (MPa)	$(\sigma_{cr})_{FEM}$ (MPa)	$(\sigma)_{cr}$ (MPa)	$(\sigma_{cr})_{EXP}$ (MPa)	$(\sigma_{cr})_{FEM}$ (MPa)
[12]	$\frac{\pi^2 t^2}{b^2}\left(\frac{\sqrt{(E_{LC}E_{TC})(1+4.1\xi)}}{6}+(2+0.62\xi^2)\left(\frac{E_{TC}\nu_L}{12}+\frac{G_L}{6}\right)\right)$	224.9	308.4	324.2	281.5	346.2	359.7
[14]	$\frac{\pi^2}{b^2 t}\left(2\sqrt{(D_L D_T)(1+4.139\xi)}+(D_{LT}+2D_S)+(2+0.62\xi^2)\right)$	225.4			282.3		
[10]	$\frac{24}{b^2}\left(1.871\sqrt{D_{11}.D_{22}}+(D_{12}+2D_{66})\right)$	274.1			325.8		
[13,15,37]	$\frac{\pi^2}{b^2}\left(4.6\sqrt{D_{11}.D_{22}}+2.67D_{12}+5.33D_{66}\right)$	282.7			336.2		

Table 5: Levels range for full factorial study on the geometric parameters of the hollow box profile.

Geometric Parameter	Level 1	Level 2	Level 3
Wall thickness (mm)	4.6	5.2	5.8
Cross-sectional aspect ratio (h/b)	1.0	1.25	1.5
Corner radii ratio (r/R)	0.5	1.0	2.0

Table 6. Levels range for full factorial study on the flange-web parameters of the hollow box profile.

Geometric Parameter	Level 1	Level 2	Level 3
Flange thickness (mm)	4.6	5.2	5.8
Web thickness (mm)	4.6	5.2	5.8
Corner radii ratio (r/R)	0.5	1.0	2.0

Table 7: Percentile contribution of each geometric parameter on the flexural behaviour of the hollow box PFRP beam.

Geometric Parameter	Flexural stiffness (EI/L^3)	Flexural strength
Wall thickness (mm)	25.43	28.75
Cross-sectional aspect ratio (h/b)	49.29	18.63
Corner radii ratio (r/R)	25.04	49.41
Error (%)	0.24	3.21
ANOVA R^2 (%)	99.76	92.79

Table 8. Percentile contribution of each flange-web parameter on the flexural behaviour of the hollow box PFRP beam.

Flange-web Parameter	Flange-web stiffness	Buckling strength
Flange slenderness (b/t_f)	25.65	19.46
Web slenderness (h/t_w)	9.52	15.03
Corner radii ratio (r/R)	64.79	61.56
Error (%)	0.04	3.95
ANOVA R^2 (%)	99.95	92.06